



Calhoun: The NPS Institutional Archive
DSpace Repository

Theses and Dissertations

1. Thesis and Dissertation Collection, all items

2014

An optical method for measuring injection timing in diesel engines, using a single port

Wyman, Sandra J.

Monterey, California: Naval Postgraduate School

<http://hdl.handle.net/10945/44031>

This publication is a work of the U.S. Government as defined in Title 17, United States Code, Section 101. Copyright protection is not available for this work in the United States.

Downloaded from NPS Archive: Calhoun



Calhoun is the Naval Postgraduate School's public access digital repository for research materials and institutional publications created by the NPS community. Calhoun is named for Professor of Mathematics Guy K. Calhoun, NPS's first appointed -- and published -- scholarly author.

Dudley Knox Library / Naval Postgraduate School
411 Dyer Road / 1 University Circle
Monterey, California USA 93943

<http://www.nps.edu/library>



NAVAL POSTGRADUATE SCHOOL

MONTEREY, CALIFORNIA

THESIS

**AN OPTICAL METHOD FOR MEASURING INJECTION
TIMING IN DIESEL ENGINES, USING A SINGLE PORT**

by

Sandra J. Wyman

September 2014

Thesis Advisor:

Knox T. Millsaps

Co-Advisor:

Douglas L. Seivwright

Approved for public release; distribution is unlimited

THIS PAGE INTENTIONALLY LEFT BLANK

REPORT DOCUMENTATION PAGE			<i>Form Approved OMB No. 0704-0188</i>	
Public reporting burden for this collection of information is estimated to average 1 hour per response, including the time for reviewing instruction, searching existing data sources, gathering and maintaining the data needed, and completing and reviewing the collection of information. Send comments regarding this burden estimate or any other aspect of this collection of information, including suggestions for reducing this burden, to Washington headquarters Services, Directorate for Information Operations and Reports, 1215 Jefferson Davis Highway, Suite 1204, Arlington, VA 22202-4302, and to the Office of Management and Budget, Paperwork Reduction Project (0704-0188) Washington DC 20503.				
1. AGENCY USE ONLY (Leave blank)		2. REPORT DATE September 2014	3. REPORT TYPE AND DATES COVERED Master's Thesis	
4. TITLE AND SUBTITLE AN OPTICAL METHOD FOR MEASURING INJECTION TIMING IN DIESEL ENGINES, USING A SINGLE PORT			5. FUNDING NUMBERS	
6. AUTHOR(S) Sandra J. Wyman				
7. PERFORMING ORGANIZATION NAME(S) AND ADDRESS(ES) Naval Postgraduate School Monterey, CA 93943-5000			8. PERFORMING ORGANIZATION REPORT NUMBER	
9. SPONSORING /MONITORING AGENCY NAME(S) AND ADDRESS(ES) Office of Naval Research			10. SPONSORING/MONITORING AGENCY REPORT NUMBER	
11. SUPPLEMENTARY NOTES The views expressed in this thesis are those of the author and do not reflect the official policy or position of the Department of Defense or the U.S. Government. IRB Protocol number ____N/A____.				
12a. DISTRIBUTION / AVAILABILITY STATEMENT Approved for public release; distribution is unlimited			12b. DISTRIBUTION CODE	
13. ABSTRACT (maximum 200 words) <p>This thesis is the design of a laser-induced fluorescence technique for use in the characterization of the fuel injection delay of various fuels, due to differences in bulk modulus. The technique is designed to work with an operational diesel engine having readily accessible glow-plug ports. The optical adapter designed for use through the glow-plug port is used as both the transmitting port for the excitation signal and the receiving port for the fluorescence signal.</p> <p>The prototype system was installed on a Detroit Diesel 3-53 two-stroke diesel engine. The beginning of the injection cycle is measured by a proximity probe set to detect injector compression to the point where the injector chamber is sealed. The actual entry of fuel into the cylinder is measured using laser induced fluorescence of an organic laser dye seeded fuel, excited by a 532-nm laser. The time/crank angle delay from the start of fuel compression to fuel entry into the cylinder can then be correlated to bulk modulus and cetane number. The combustion event can also be detected using the same optics and its timing correlated with known fuel properties.</p>				
14. SUBJECT TERMS Hydroprocessed Renewable Diesel, HRD, Alternative Fuel Blends, F-76, Diesel Engine Combustion, Diesel Engine Injection Timing, Cetane Number, Bulk Modulus, Laser Fluorescence Measurement, Pyromethene 597, Diesel Engine Combustion Timing, Laser-Induced Fluorescence, Fiber Optic, Sapphire Optic, Spectroscopy			15. NUMBER OF PAGES 99	
			16. PRICE CODE	
17. SECURITY CLASSIFICATION OF REPORT Unclassified	18. SECURITY CLASSIFICATION OF THIS PAGE Unclassified	19. SECURITY CLASSIFICATION OF ABSTRACT Unclassified	20. LIMITATION OF ABSTRACT UU	

NSN 7540-01-280-5500

Standard Form 298 (Rev. 2-89)
Prescribed by ANSI Std. Z39-18

THIS PAGE INTENTIONALLY LEFT BLANK

Approved for public release; distribution is unlimited

**AN OPTICAL METHOD FOR MEASURING INJECTION TIMING IN DIESEL
ENGINES, USING A SINGLE PORT**

Sandra J. Wyman
Lieutenant, United States Navy
B.S.E., University of Michigan, 2007

Submitted in partial fulfillment of the
requirements for the degree of

MASTER OF SCIENCE IN MECHANICAL ENGINEERING

from the

**NAVAL POSTGRADUATE SCHOOL
September 2014**

Author: Sandra J. Wyman

Approved by: Knox T. Millsaps
Thesis Advisor

Douglas L. Seivwright
Co-Advisor

Garth V. Hobson
Chair, Department of Mechanical and Aerospace Engineering

THIS PAGE INTENTIONALLY LEFT BLANK

ABSTRACT

This thesis is the design of a laser-induced fluorescence technique for use in the characterization of the fuel injection delay of various fuels, due to differences in bulk modulus. The technique is designed to work with an operational diesel engine having readily accessible glow-plug ports. The optical adapter designed for use through the glow-plug port is used as both the transmitting port for the excitation signal and the receiving port for the fluorescence signal.

The prototype system was installed on a Detroit Diesel 3–53 two-stroke diesel engine. The beginning of the injection cycle is measured by a proximity probe set to detect injector compression to the point where the injector chamber is sealed. The actual entry of fuel into the cylinder is measured using laser induced fluorescence of an organic laser dye seeded fuel, excited by a 532-nm laser. The time/crank angle delay from the start of fuel compression to fuel entry into the cylinder can then be correlated to bulk modulus and cetane number. The combustion event can also be detected using the same optics and its timing correlated with known fuel properties.

THIS PAGE INTENTIONALLY LEFT BLANK

TABLE OF CONTENTS

I.	INTRODUCTION AND BACKGROUND.....	1
A.	NAVY FUEL CONSUMPTION.....	1
B.	BENEFITS AND KNOWN ISSUES OF BIOFUELS	1
C.	UNIQUE PROPERTIES OF HYDROPROCESSED RENEWABLE DIESEL AND SYNTHETIC PARAFFINIC KEROSENE	2
D.	FLEET FUEL UTILIZATION.....	4
E.	BULK MODULUS.....	4
F.	CETANE NUMBER	5
G.	OTHER FUEL PROPERTIES.....	6
H.	OBJECTIVES	7
II.	LITERATURE REVIEW	9
A.	HYDROPROCESSED RENEWABLE DIESEL EFFECTS ON ENGINE PERFORMANCE	9
B.	FISCHER-TROPSCH DIESEL AND SYNTHETIC PARAFFINIC KEROSENE EFFECTS ON ENGINE PERFORMANCE	10
C.	VARIABILITY OF BULK MODULUS AND OTHER PHYSICAL PROPERTIES WITH FUEL FEED STOCK SOURCE AND ITS EFFECT ON ENGINE PERFORMANCE	12
D.	UNCERTAINTY IN LITERATURE.....	16
III.	EXPERIMENTAL DESIGN.....	17
A.	GENERAL OVERVIEW	17
B.	LASER FLUORESCENCE	18
C.	EXPERIMENTAL SETUP	22
1.	Engine.....	23
2.	Displacement Sensor	24
3.	Sapphire Rod Assembly	26
a.	<i>Sapphire Rod</i>	27
b.	<i>Upper and Lower Rod Housings</i>	27
c.	<i>Assembly Sleeve</i>	28
4.	External Instrument Bracket.....	29
5.	Laser.....	31
6.	Lens-Sensor Assembly	31
a.	<i>Dichroic Mirror</i>	33
b.	<i>Sensor</i>	33
c.	<i>Filter</i>	34
d.	<i>Fiber Optic Cables</i>	35
e.	<i>Collimation Lenses</i>	36
7.	Oscilloscope	37
IV.	DESIGN SPECIFICATIONS AND CHALLENGES.....	39
A.	DESIGN CONSTRAINTS	39
B.	INITIAL DESIGN AND CHALLENGES	39

IV. RESULTS AND DISCUSSION	43
V. CONCLUSIONS AND OBSERVATIONS.....	49
VI. FUTURE WORK.....	51
APPENDIX A. E2E-CR8C2 DISPLACEMENT SENSOR SPECIFICATION.....	53
APPENDIX B. DISPLACEMENT SENSOR BRACKET DRAWINGS.....	55
APPENDIX C. SAPPHIRE ROD DRAWING.....	59
APPENDIX D. UPPER ROD HOUSING DRAWINGS	61
APPENDIX E. LOWER ROD HOUSING DRAWINGS.....	63
APPENDIX F. SLEEVE DRAWINGS	65
APPENDIX G. INSTRUMENT BRACKET DRAWINGS	67
APPENDIX H. COLLIMATION LENSES.....	69
APPENDIX I. HR 2000 SPECTROMETER SPECIFICATIONS.....	71
APPENDIX J. SONY CCD LINEAR IMAGE SENSOR DATA SHEET	75
LIST OF REFERENCES	77
INITIAL DISTRIBUTION LIST	81

LIST OF FIGURES

Figure 1.	Injection line pressure for two soy based biodiesels, HPVB and LPVB, their 20% blends with conventional fuel and conventional diesel fuel versus crank angle degrees. Data taken from a John Deere 4276T equipped with a distributor-type injection pump, from [27].	13
Figure 2.	Concept Map of NO emissions and combustion characteristics from [29]	15
Figure 3.	Sample cylinder pressure vs. CAD curve with an overlay of the injection and combustion delays.	18
Figure 4.	A graphical representation of laser induced fluorescence, showing an excitation wave length in green and the fluorescent response at a lower, orange, wave length, after [31].	19
Figure 5.	Absorption and emissions spectra for pyrromethene 597 dissolved in gasoline, after [33].	20
Figure 6.	Absorption (bold lines) and fluorescence (thin lines) spectra of pyrromethene 597 at 2×10^{-6} M in isooctane (a) and 2,2,2-trifluoroethanol (b). Intensity is normalized to the fluorescence quantum yield, from [32].	20
Figure 7.	The 532 nm laser exciting a response from F-76 seeded with pyrromethene 597.	21
Figure 8.	Schematic view of the displacement sensor, laser sapphire rod, and dyed fuel spray. after [35].	22
Figure 9.	Schematic of the complete experimental set-up, showing the relationship of the engine mounted sensors to the free-standing optics assembly, signal generating laser, and signal processing oscilloscope and computer, after [35].	23
Figure 14.	Sapphire rod, upper and lower rod housings with PTFE ferrules, and collimator lens.	27
Figure 16.	Section view of the complete sapphire rod assembly showing the rod, upper and lower housings and the sleeve.	29
Figure 17.	External instrument bracket shown mounted to a Detroit Diesel 3–53 exhaust manifold.	30
Figure 18.	Photos of the instrument bracket mounted to the Detroit Diesel 3–53 and section view, produced in Solidworks, from the left side showing the complete sapphire rod assembly mounted in the engine.	31
Figure 19.	Catalog image of a CM1 series cage-cube from [36].	32
Figure 20.	External photo of the complete lens-sensor assembly, green arrows indicate excitation signal, orange arrows indicate the response signal, and a section view of the same assembly produced in Solidworks, illustrating the internal light path.	32
Figure 21.	Transmission and reflectance for DMLP567 series dichroic filter in response to s-polarized light, after [41].	33
Figure 22.	Response curve for PDA36A Switchable Gain Detector from [42].	34
Figure 24.	Attenuation curves for 0.39 NA, 800nm fiber optics from [44].	35
Figure 25.	Attenuation curves for 0.48 NA, 400nm fiber optics from [45].	36

Figure 26.	Solidworks model of original design showing optics mounted on the instrument bracket.....	40
Figure 27.	Section view of the cylinder head with the location of the engine seal and the need to ensure adequate clearance between the piston and the sapphire rod at TDC highlighted.	41
Figure 28.	The original design iteration included a large air gap, welded fabrication of the instrument bracket, and a sapphire rod of low quality material.	42
Figure 29.	The left image show the fluorescence response from a jar of fuel reaching the sensor, the right image shows no response reaching the sensor when the fuel is moved away.	43
Figure 30.	Unfiltered signal reaching the sensor though the dichroic mirror, a large amount of green 532 nm leakage is shown, with the bluish center portion being the mingling of the yellow fluorescence signal and the leakage.....	44
Figure 31.	Numerical aperture loss, if the aperture on the sending side is greater than the aperture on the receiving side, some signal may reflect back through the system.....	44

LIST OF TABLES

Table 1.	Bulk Modulus of SPK, HRD, F-76, and 50/50 Blends of F-76 with HRD and SPK.	5
Table 2.	Cetane Number of SPK, HRD, F-76, and 50/50 blends of F-76 with HRD and SPK, from [15].	6
Table 3.	A breakdown of fuel type showing composition by percent paraffin, olefin, and aromatics from [5].	7
Table 4.	Specifications for Detroit Diesel 3–53 from [36].	24
Table 5.	Laser Transmission Rod Specifications from [37]	27
Table 6.	Specifications for Laser from [35]	31

THIS PAGE INTENTIONALLY LEFT BLANK

LIST OF ACRONYMS AND ABBREVIATIONS

3-D	three-dimensional
AFRL	Air Force Research Laboratories
B100	100% Biodiesel
B80	80% Biodiesel 20% conventional diesel fuel
B20	20% Biodiesel 80% conventional diesel fuel
BSFC	break specific fuel consumption
CA	crank angle
cm	centimeters
CNC	Computer Numerical Control
Corp	corporation
dB	decibel
DoD	Department of Defense
DI	Direct Injection
EGR	exhaust gas recirculation
FAEE	fatty acid ethyl esters
FAME	fatty acid methyl esters
Ft-lbs	foot-pounds
FY	Fiscal Year
GTL	gas to liquid
HEM	Heat exchanger method
Hp	horsepower
HRD	hydroprocessed renewable Diesel
HVO	hydroprocessed vegetable oil
IGD	ignition delay
in.	inches
Inc.	Incorporated
IVC	intake valve closing
kHz	Kilohertz
kPa	Kilopascal
ksi	Kilopound per square inch
$\lambda_{A \text{ max}}$	peak absorption wavelength
$\lambda_{F \text{ max}}$	peak fluorescence wavelength
lb _m	pound
LIF	laser induced fluorescence
<i>M</i>	molar mass (kg/mol)
mm	millimeter

MPa	Mega Pascal
MPL	Marine Propulsion Lab
Ms	milliseconds
mV	Millivolt
N	Newtons
NA	Numerical Aperture
NATO	North Atlantic Treaty Organization
Nm	Nanometer
NO	nitric oxide
NO _x	nitric oxide and nitrogen dioxide
Ns	nanosecond
OEM	original equipment manufacturer
ONR	Office of Naval Research
Psi	pound per square inch
PTFE	polytetrafluoroethylene
Rpm	revolutions per minute
SOC	start of combustion
SOI	start of injection
SPK	synthetic paraffinic kerosene
SwRI	Southwest Research Institute
TDC	top dead center
ULSD	ultra-low sulfur diesel fuel

ACKNOWLEDGMENTS

Thank you to my thesis advisors, Dr. Knox Millsaps and Douglas Seivwright, for the opportunity to be a part of this project. Your support and advice kept me on course through many setbacks. It has been a learning experience that I will carry with me to future endeavors.

Thank you to John Mobley, Model Maker, and Robert Wright, Research Associate, whose creativity and technical expertise made this project possible, and to Kyle Reed, NRIEP student, whose Solidworks model saved me many hours of work.

Thank you to Dr. Sharon Beerman-Curtin from the Office of Naval Research (ONR), who sponsored this program, and Dr. James (Tim) Edwards of the Air Force research Laboratories (AFRL), who supplied the Synthetic Paraffinic Kerosene (SPK) fuel.

Also, a special thanks to my friend and mentor, Dr. John F. Copeland, DABR(ret), for his constant encouragement and reassurance, and occasional brilliant ideas kept me on track.

Further thanks to Sue Hawethorne of the thesis processing office, whose keen eye for detail and comma placement helped make this document what it is.

THIS PAGE INTENTIONALLY LEFT BLANK

I. INTRODUCTION AND BACKGROUND

A. NAVY FUEL CONSUMPTION

The Department of Defense is the single largest energy user in the nation, purchasing approximately 60% percent of its FY 2012 fuel needs from outside the United States [1].

With a projected fuel consumption for FY 2013 of over 114 million barrels and over 75 % of Department of the Navy fuel resources going to meet operational needs; the navy rightly views energy as a vital strategic resource [1, 2]. The Secretary of the Navy has set a Department wide goal to reduce non-tactical petroleum use by 50% by 2015 and to source approximately 50% of Department of the Navy energy requirements from alternative sources by 2020 [2]. A major piece of the puzzle in meeting these goals is developing alternative fuels that are compatible with current naval platforms and are “drop-in” replacements for JP-5 and NATO F-76, the current fleet standards. However, the use of seawater compensated shipboard storage tanks, legacy engine technology, high flash point requirements of 60°C (140°F) minimum, and need for long term fuel storage pose challenges to the use of conventional methylated and ethylated vegetable oil, otherwise known as fatty acid methyl ester (FAME) and fatty acid ethyl ester (FAEE) biofuel. Throughout this paper FAME will be used to refer to all such fuels.

B. BENEFITS AND KNOWN ISSUES OF BIOFUELS

Currently, blends of FAME biofuel and number two diesel fuel are readily available to the public in concentrations of up to 80% biofuel (B80). Most automobile and heavy equipment manufacturers have approved blends of up to 20% biofuel (B20) for use in their engines without any modifications. Biodiesel and biodiesel blends have the following benefits over standard petroleum derived fuel:

- Reduced wear on metallic engine components
- Reduced emissions of particulate matter, sulfur dioxide, carbon monoxide and unburned hydrocarbons

- Reduced life cycle carbon dioxide emissions
- Reduced cost in certain markets
- Readily produced from widely available crop wastes or purpose grown crops

Unfortunately, traditional biofuels also have several drawbacks that make them unsuitable for use in naval applications. Among them are:

- Increased susceptibility to biofouling in seawater compensated tanks
- Poor long-term storage due to product oxidation
- Incompatibility with certain plastic and rubber engine components
- Formation of water-fuel emulsions in fuel handling systems
- Slightly increased nitrous oxide emissions
- Higher specific fuel consumption
- Highly variable product characteristics and quality dependent on feed stock and production methods

Several of these issues can be addressed through the use of synthetic paraffinic kerosene (SPK) or hydroprocessed renewable diesel (HRD) and their blends with standard military fuels (F-76 and JP-5). The low aromatic and high paraffin content of these fuels means that they are stable in long term storage, do not readily emulsify with water, and resist bio-contamination.

C. UNIQUE PROPERTIES OF HYDROPROCESSED RENEWABLE DIESEL AND SYNTHETIC PARAFFINIC KEROSENE

HRD, also known as either hydrotreated or hydroprocessed renewable diesel, is a second-generation biofuel. It can be produced from a wide range of biologically based oils, including animal fats, and plant-based oils and is miscible with F-76. During the hydrotreating process, oil fractions are reacted with hydrogen and a series of proprietary catalysts, removing oxygen from the long chain hydrocarbon molecules of the fuel. The

resulting product has none of the long-term storage and handling issues associated FAME based fuel, due to a very low concentration of aromatics and oxygenates [3].

Fuel produced this way typically has a high cetane number, leading to more rapid auto ignition and fewer exhaust particulates than traditional petroleum-based fuels. The hydrotreating process is regularly used by petroleum refineries in the production of ultra-low sulfur diesel fuels and cold weather optimized fuel blends; as such, much of the costly infrastructure required to produce HRD on a large scale is already in place. Unfortunately, many original equipment manufacturers (OEMs) are unfamiliar with the performance of high cetane number fuels in their machinery and are uncomfortable certifying it for use. The sample used in this paper (HRD-76) was obtained from the Naval Air Systems Command, Fuels Division, Patuxent River, MD. It was produced from algae based oil and has a cetane number of 78; for comparison the average cetane number for F-76 is 46 [4, 5].

SPK, produced using the Fischer-Tropsch process, was originally derived in Germany in the 1920s and 1930s in response to fuel shortages. The initial step in the process is the gasification of a feedstock fuel to produce carbon dioxide, carbon monoxide and hydrogen gas. Typically, coal or natural gas is used as the carbon-hydrogen feedstock; however, biologically based oils and methane may also be used. The second step involves reacting steam with carbon monoxide to produce more hydrogen gas and achieve the desired carbon/hydrogen ratio. Lastly, reaction with a catalyst allows the formation of various long chain hydrocarbons. Much like hydro-treated fuels, the fuel produced via the Fischer-Tropsch process lacks both aromatics and oxygenates and has none of the long-term storage and handling issues associated with FAME-based fuels. It is also free of sulfur, vanadium, and other contaminants. Various formulations of SPK have been successfully tested for use in aircraft as a replacement for JP-5 and its civilian counterpart Jet-A [6]. This fuel typically has a rather low cetane number, and as with its counterpart HRD-76, many OEMs are uncomfortable certifying its use in their equipment. The sample used in this paper is provided by Dr. (Tim) James Edwards of Wright Patterson Air Force Research Laboratories and has a cetane number of 24 [5,7].

D. FLEET FUEL UTILIZATION

The U.S. Naval fleet relies upon two primary fuels, F-76 and JP-5, to meet its needs across a wide variety of operational platforms. Both fuels have been standardized to perform well in military storage and handling systems, meet shipboard safety requirements, and tolerate seawater contamination.

However, JP-5 and F-76 were developed to meet very different operational needs. JP-5, and other kerosene-based jet fuels, such as JP-8 and Jet-A, are used almost exclusively in gas turbine engines, where combustion is a continuous steady-state event. In contrast, F-76 must function well in gas turbines, steam boilers, and diesel engines. Specifically, the challenge is in meeting the requirements for satisfactory continual use in diesel engines, where combustion is a transient event that must be continually reproduced with precise event timing. It is the effect of various fuel properties on event timing that the proposed technique is intended to study.

E. BULK MODULUS

Bulk Modulus is a measure of a substance's resistance to uniform compression and is defined as $K = -V \frac{dP}{dV}$, the ratio of pressure to volumetric strain. Equivalently it can be defined as $K = \rho \frac{dP}{d\rho}$ where ρ is the density and $\frac{dP}{d\rho}$ is the derivative of pressure with respect to density. For a fluid, the bulk modulus, K , and the density ρ define the speed of sound, c , and other mechanical waves, including pressure, where $K = \frac{c^2}{\rho}$ [8].

Bulk modulus is of particular concern in engine timing. A higher bulk modulus of compressibility results in a higher speed of sound in the fuel blend, and thus the pressure wave generated when the rocker arm impacts the injector. This leads to an earlier entry of fuel into the combustion cylinder by as much 1.0 crank angle (CA degrees) when using B100 (a 100% methyl soyate, FAME-type fuel) [9]. The advanced injection timing results in the 2–4% increase in NO_x emissions often seen when using FAME biofuel blends. Conversely, a low bulk modulus has the opposite effect, retarding injection

timing by as much as 0.5 CA degrees, as seen when using NorPar-13, a paraffinic hydrocarbon with a particularly low bulk modulus of approximately 1,200 MPa (174 ksi) at 3.45 MPa (500 psi) [7]. The retarded injection timing reduces NO_x formation, but can lead to poor combustion and greater soot formation [10, 11].

Table 1, shows the bulk moduli of SPK, HRD, F-76 and 50/50 blends of F-76 which each of the alternative fuels. As a reference, the bulk modulus for water is approximately 2150 MPa (311.8 ksi) and the bulk modulus of mercury is approximately 28,500 MPa (4133.6 ksi) [12].

Table 1. Bulk Modulus of SPK, HRD, F-76, and 50/50 Blends of F-76 with HRD and SPK.

Fuel					
Bulk Modulus (MPa)	SPK	50%SPK/ 50% F-76	HRD	50%HRD/ 50% F-76	F-76
	¹ 1258	² 1343	³ 1400	³ 1414	³ 1428

Note 1: Found in literature [13]. Awaiting specific sample test results from SWRI. Note 2: Estimated using a linear model. Note 3: As measured by SWRI at 23.5°C (74.3°F) and 3.45 MPa (500 psi), [14].

The range in bulk moduli shown in Table 1, (1258 MPa to 1428 MPa), while not terribly large, is great enough to impact fuel behavior within and engine's injection system.

F. CETANE NUMBER

Cetane number is a measure of how readily a fuel auto ignites. This is of particular concern for fuel combustion timing, with a high cetane number indicating a shorter ignition delay. High cetane number fuels have been correlated with a slower rate of pressure rise and a lower peak pressure during combustion [5]. This results in less overall stress on engine components. Table 2 lists the cetane numbers for SPK, F-76, HRD, and 50/50 blends of F-76 with both alternative fuels.

Table 2. Cetane Number of SPK, HRD, F-76, and 50/50 blends of F-76 with HRD and SPK, from [15].

Fuel					
Cetane Number	SPK	50%SPK/ 50% F-76	F-76	50%HRD/ 50% F-76	HRD
	24	35	46	66	78

Low cetane number fuels can be problematic for diesel engines, resulting in a significant combustion delay followed by a swift, sharp rise in pressure that results in a higher stress on engine components [5]. Low cetane fuels have also been linked to high levels of NO_x and particulate matter in exhaust [10]. A previous study reported that the Detroit Diesel 3–53 in the Naval Postgraduate Schools' Marine Propulsion Laboratory (MPL) would not operate on blends containing greater than 50 % SPK [16].

Cetane number and bulk modulus can have competing effects; research conducted at the University of Pennsylvania Energy Institute shows that a Fischer-Tropsch fuel with high cetane number and low bulk modulus produces retarded injection timing, followed by a minimal injection delay, resulting in low NO_x formation, low particulate matter emissions, and gradual cylinder pressure rise [11].

G. OTHER FUEL PROPERTIES

Another relevant fuel property when examining injection timing and the operation of fuel injectors and fuel pumps is lubricity. Lubricity is a measure of a lubricant's performance in a system and is not a material property; it is usually specified in terms of the degree of wear scarring that occurs between two fuel-coated metal parts as they come in contact. The lubricating properties of a fuel are particularly important for the operation of fuel pumps and injectors where the fuel itself, not the engine oil, serves to lubricate the moving parts as it moves through the system. Low lubricity fuel has been shown to cause high wear and scarring [17]. Hydrotreatment of conventional diesel fuels to reduce sulfur content and improve stability has had the unintended consequence of also removing the olefins and aromatics that contribute to lubricity [17]. It can be expected that both HRD, which undergoes a similar hydrotreatment process and SPK which is purposefully

formulated for a low aromatic and olefin content will exhibit low lubricity and impact injection system behavior. Table 3 breaks down the three fuels of interest by percent paraffin, olefin and aromatic content.

Table 3. A breakdown of fuel type showing composition by percent paraffin, olefin, and aromatics from [5].

Fuel Composition			
Fuel Type	F-76	HRD	SPK
% paraffin	70.7	98.5	94.3
% olefin	2.3	0.9	4.7
% aromatics	27	0.6	1.0

H. OBJECTIVES

This thesis had four primary objectives. The first was to develop an optical method for determining the start of fuel injection into the combustion cylinder of an operational diesel engine. The second goal was to further refine the optical instrumentation and measurement techniques to allow the measurement of the initiation of combustion. The third objective was to design, manufacture, and install the mechanical components necessary to mate the optical equipment with the Detroit Diesel 3–53 in the Naval Postgraduate School’s Marine Propulsion Laboratory. Finally, this project aimed to modify the subject engine to allow the timing of the initiation of injection, the entry of fuel into the combustion cylinder, and the initiation of combustion in crank angle degrees.

THIS PAGE INTENTIONALLY LEFT BLANK

II. LITERATURE REVIEW

A. HYDROPROCESSED RENEWABLE DIESEL EFFECTS ON ENGINE PERFORMANCE

Previous experimental work with hydroprocessed diesel fuels in direct injection diesel engines has generally shown satisfactory performance.

Peterson et al. [5] tested HRD-76 in a two-stroke, direct injection, naturally aspirated marine diesel engine with mechanical unit injectors and showed satisfactory results with blends ranging from 25% HRD/75% F-76 to 100% HRD. An increased proportion of HRD resulted in an increased cetane number, a decreased ignition delay (IGD) and lower peak pressure and rate of pressure rise. The summary effect was that the high cetane number fuel blends resulted in reduced structural fatigue, vibration, and noise.

Sugiyama et al. [18] tested a hydrotreated vegetable oil (HVO) in a direct injection, turbocharged, automotive diesel and found both decreased smoke and particulate matter emissions as well as reduced fuel consumption (up to 5%) as compared with conventional diesel fuel. Sugiyama's study found improved combustion and concluded that HVO can be adopted for use in direct injection diesel engines over a wide range of blend ratios.

Kuronen et al. [19] compared HVO to a European specification sulfur-free conventional diesel (EN 590) in two heavy-duty engines and two city buses. The effect on emissions of the HVO was a 14% percent reduction in NO_x, a 46 % reduction in particulate matter, and 78% reduction in carbon monoxide (CO). However, due to the lower density of HVO, volumetric fuel consumption was 5–6% higher than with conventional fuel [19].

Murtonen et al. [20] conducted a similar study in 2010, examining EN590, HVO, FAME and a high cetane number gas-to-liquid (GTL) or Fischer-Tropsch process fuel. This study found that, with the exception of NO_x emissions from FAME, all emissions

considered harmful to human health were significantly reduced when using alternative fuels [20].

Happonen et al. [21] took the investigation into the performance of hydrotreated fuel one step further by adjusting various engine parameters to optimize emissions performance. By testing different combinations of advanced intake valve closing (IVC), exhaust gas recirculation (EGR) percentage, injection pressure (P_{inj}), and start-of-injection timing (SOI) at 50%, 75%, and 100% loads, Happonen was able to conclude that it is possible to achieve a low particulate matter/low NO_x emissions condition. This was achieved with advanced IVC, a small percentage of EGR and by increasing injection pressure 30–70 % depending on load. The result was that NO_x emission was decreased 30–50%, depending on load, and particulate matter by 25–33% E [21].

These studies establish the potential for one formulation of hydrotreated fuel to perform acceptably well in terms of engine emissions, fuel consumption, and structural fatigue.

B. FISCHER-TROPSCH DIESEL AND SYNTHETIC PARAFFINIC KEROSENE EFFECTS ON ENGINE PERFORMANCE

Although Fischer-Tropsch fuels in general have undergone extensive testing in gas turbine and diesel engines, previous experimental work with low cetane, SPK like fuels in direct injection diesel engines is somewhat limited. What work has been conducted, shows a positive effect on engine emissions largely due to the low aromatic and sulfur content of the fuel. Studies using high cetane number formulations generally show satisfactory performance, while those using low cetane number formulations demonstrate the high IGD and rough performance found with other types of low cetane fuel.

Petersen et al. [5] tested an SPK with a cetane number of 24 in the Detroit Diesel 3–53 marine diesel engine located at the Naval Postgraduate School. The SPK was blended with F-76 in ratios from 25% SPK/75% F-76 to 100% SPK. An increase in the proportion of SPK resulted in a lower cetane number and an increased IGD, with a peak IGD of 0.50–0.75 ms with 100% SPK versus F-76. Similarly, an increased proportion of

SPK also showed a higher peak cylinder pressure and rate of pressure rise. The summary effect was that the low cetane number fuel blends resulted in a longer IGD with a more rapid combustion and higher peak pressure, leading to greater structural stress on the engine and rough performance [5].

Abu-Jrai et al. [22] studied blends of ultra-low sulfur diesel (ULSD) with GTL in up to a 50/50 blend by volume. The study was carried out using a Lister Petter TR1, single cylinder experimental engine and showed that GTL or the 50/50 blend did not impact the start of combustion compared to the conventional diesel fuel. It did, however, report a significantly reduced proportion of fuel burned in the pre-mixed combustion phase, especially during high-load operations. This resulted in lower peak cylinder pressures and combustion temperatures. A second similar study by Abu-Jrai et al. [23] showed a slight injection delay for GTL when using a common rail injection system. This was attributed to the lower density and higher bulk modulus of GTL when compared to diesel fuel. The injection delay in conjunction with the reduced pre-mixed combustion phase resulted in a lower peak cylinder pressure, a lower maximum rate of pressure rise, and a lower maximum rate of heat release, but contradictorily no increased soot formation. It was concluded that the reduction in ignition delay from the higher cetane number and retarded SOI shift the combustion balance, resulting in less pronounced pre-mixed combustion phase but without shifting the start of combustion [23].

Lin et al. [24] performed a combustion analysis of a synthetic, Fischer-Tropsch-derived jet fuel (S-8) very similar to SPK. They concluded that the S-8 had very similar two-stage ignition characteristics to its military fuel equivalent JP-8, but a shorter ignition delay. Further, the study concluded that while the synthetic jet fuel had very similar spray and atomization characteristics to conventional jet fuel, the potential lubrication and sealing problems fostered by the absence of aromatics need to be weighed against any benefit from reduction in soot formation. This observation is in line with Navy experience in using military jet fuels (JP-5 and JP-8), both with a moderate aromatic content, in diesel engines [25].

Moses [26] reported extensively on the comparative properties of several semi-synthetic jet fuels, which are blends of SPK and conventional jet fuel. All five SPK fuels

studied, produced very similar semi-synthetic jet fuels when blended 50/50 with conventional jet fuel. The five test fuels were chosen specifically to cover a large range of SPK compositions likely to result from the Fischer-Tropsch process. Moses [26] concludes that with the exception of lubricity and elastomer compatibility, all the property variations among semi-synthetic jet fuels were within the world-wide range for conventional jet fuel [26]. While not directly related to SPK performance in diesel engines, it can be inferred from this work that blends of SPK-type fuels should perform similarly to other low cetane, kerosene type fuels. Further, much like JP-8 and JP-5, SPK fuels likely require lubricity enchantment in order to reduce engine wear and tear.

These studies establish that high cetane Fischer-Tropsch fuels can be expected to show a positive effect on engine emissions largely due to the low aromatic and sulfur content of the fuel. Further, some formulations that combine a high cetane number with low bulk modulus have shown a retarded injection and shift in the combustion balance, without affecting the actual combustion timing. This resulted in favorable low soot and low NO_x emissions. Low cetane number formulations originally developed as synthetic jet fuel, likely require lubricity enchantment but otherwise should be expected to perform similarly to the jet fuels they are intended to replace.

C. VARIABILITY OF BULK MODULUS AND OTHER PHYSICAL PROPERTIES WITH FUEL FEED STOCK SOURCE AND ITS EFFECT ON ENGINE PERFORMANCE

A great deal of research has been conducted on the impacts of the properties of various FAME type fuels on engine performance, and general consensus exists on the impact of cetane number on fuel combustion. Less understood is the interaction between bulk modulus, viscosity, and density of a given fuel formulation with a specific type of fuel injection system.

Boehman et al. [9] investigated the interaction between the bulk modulus and fuel injection timing using samples that included unrefined soybean oil, soy-oil based biodiesel, a paraffinic distillate (Norpar-13), ultra-low sulfur diesel fuel, and conventional diesel fuel. A positive correlation was found between the higher bulk modulus of vegetable oils and the biodiesel derived from them, and an advance in

injection timing. A 1.0 CA degree advance was noted when using B100 versus conventional diesel. The opposite trend was noted when using low bulk modulus paraffinic fuels, with a retardation of 0.5 CA degrees for Norpar-13. Further, it was concluded that the advance in injection timing seem with FAME-type biofuels causes the increase in NO_x emissions also seen with such fuels. This study also presented data showing the dependence of FAME fuel bulk modulus based on the feedstock. Values ranged from a high of 1688 MPa (measured at 40°C and 6.89 MPa) for methyl linolenate to 1489 MPa (measured at 40°C and 6.89 MPa) for methyl laurate [9].

Tat and Van Gerpen [27] measured the density and speed of sound, calculating the bulk modulus for 21 esters and ester blends. Showing that the injection pressure pulse for biodiesel was 1.5–2.0 CA degrees advanced from that of conventional diesel fuel for a fixed injection pump system, they attributed 0.45 to 0.68 CA degrees of the timing advance to the 169 MPa difference in the bulk modulus. Figure 1 shows the injection line pressure versus CA degrees for two particular soy-based bio diesels and their blends with conventional diesel fuel.

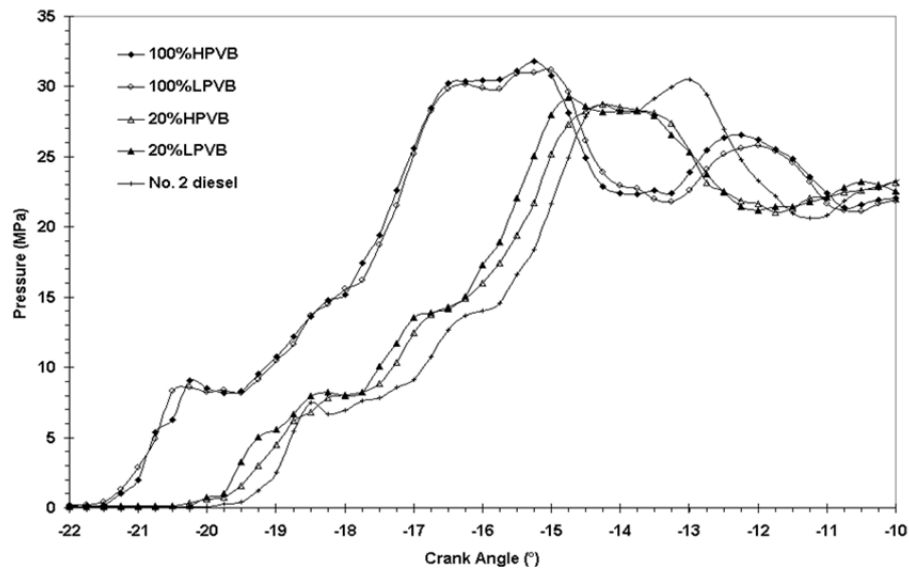


Figure 1. Injection line pressure for two soy based biodiesels, HPVB and LPVB, their 20% blends with conventional fuel and conventional diesel fuel versus crank angle degrees. Data taken from a John Deere 4276T equipped with a distributer-type injection pump, from [27].

Tat and Van Gerpen [27], further showed density, speed of sound, and therefore bulk modulus increase as the degree of unsaturation of the fuel components increases, although the increase is uniform with each additional double bond added. Examining several variations on fuel injector technology, they further concluded that the mechanical unit injectors found throughout the naval fleet and on the Detroit Diesel 3–53 in the Naval Postgraduate School Marine Propulsion Lab are likely to be less sensitive to variations in bulk modulus than new pump-in-line systems or those using state-of-the-art electronic unit injectors.

In a second study, Boehman et al. [28] used a single cylinder engine to examine the impacts on injection timing in a pump-line-nozzle system of blending Fischer-Tropsch derived diesel fuel with low sulfur, ultra-low sulfur and biodiesel fuels. The study contradicted Tat and Van Gerpen’s conclusions that a mechanical fuel injection system is less sensitive to variations in fuel bulk modulus than an electronically controlled system [27, 28]. Examining data from a Cummins ISB 5.9L turbodiesel with a Bosch electronically controlled fuel system they saw only a 0.2 CA degree advance in injection timing for a 50/50 blend of low sulfur diesel fuel and B20. This is in contrast to the 0.5 CA degree advance seen with a purely mechanical system. It was concluded that the engine controller may shift injection timing due to differences in position required to meet the load conditions while accounting for differences in heating value and cetane number among the test fuels [28]. Using a Yanmar L70EE DI diesel engine, the same group examined the impact of a high cetane Fischer-Tropsch fuel on NO_x and CO emissions, brake specific fuel consumption (BSFC) and injector needle lift signal. It was shown that the addition of a high cetane, low bulk modulus fuel retarded injection timing and advanced combustion timing relative to the base fuels. Further, the “late” injection timing blends showed lower peak pressure, lower CO emissions, and lower BSFC with only a modest increase in NO_x [28].

Tat, Wang, and Van Gerpen [29] investigated the lower heating value, volatility, density, speed of sound, bulk modulus, and cetane number of various biodiesel formulations. They concluded that approximately half the start of combustion (SOC) advance associated with both soybean oil methyl ester and yellow grease methyl ester

biodiesel originated with a SOI advance. This was due both to the distributor type fuel injecting more fuel to compensate for the 12 % lower heating value of biodiesel and the effect of the fuels' bulk modulus, viscosity, and density. When controlling for temperature, it was found that the delivery of bio-diesel was still higher than conventional fuel due to increased viscosity. When controlling for viscosity, the opposite proved to be true, with the delivery of conventional diesel fuel being greater than that of biodiesel. This was caused by the metering orifices in the fuel injection pumps restricting the fuel flow for more dense fuels. The remainder of SOC advance was due to the higher cetane number of the biodiesel [29]. Figure 2 is a concept map showing the interplay between cetane number, combustion timing, injection timing, fuel physical properties, and the production of NO. It is a visual summary of the tug-of-war between competing effects driving combustion and ultimately engine performance.

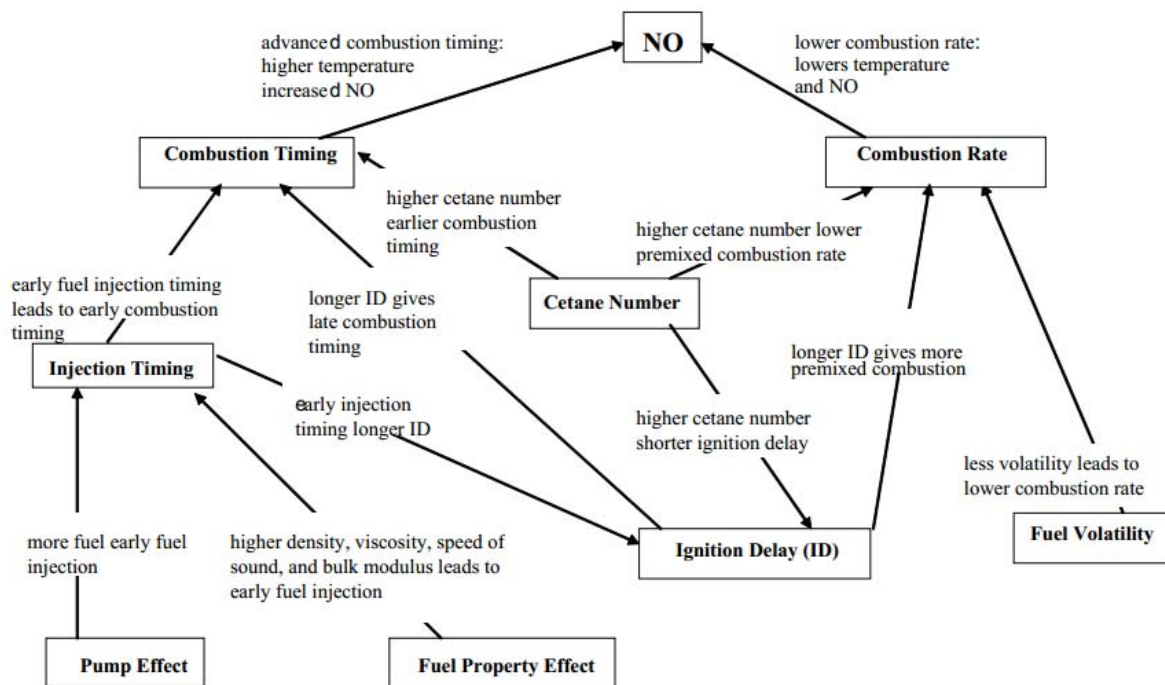


Figure 2. Concept Map of NO emissions and combustion characteristics from [29]

These studies show that although the effect of cetane number on SOC is well understood, the interplay of bulk modulus, viscosity, density, and injection system type with a fuel's auto-ignition potential needs to be better characterized and more specifically, is not known for HRD.

D. UNCERTAINTY IN LITERATURE

Although the general effects of bulk modulus and cetane number on injection timing and combustion timing are understood, there interaction with, and overall impact on the performance of a two-stroke marine diesel is not. Such research is generally conducted using a single cylinder engine. Further, the behavior of a fully mechanical two-stroke engine such as those commonly found aboard U.S. naval vessels, running on either a hydroprocessed renewable fuel or a synthetic fuel is not well characterized as most research is focused on newer engine technologies.

III. EXPERIMENTAL DESIGN

A. GENERAL OVERVIEW

The purpose of the laser-based fluorescence technique proposed in this study is to determine the start of injection of fuel into the combustion cylinder. In conjunction with a proximity probe set to indicate when the injector plunger has sealed the injector chamber and a positive force is being applied to the fuel charge, the two events bracket the injection process and allow for a means to measure the plunger engagement, injection period, and start of injection into the cylinder with respect to crank-angle-rotation via an optical encoder. Bench-top measurements found that the chamber sealed when approximately .3620 cm (0.1425 in.) of plunger depression occurs for the N50 injectors currently installed on the MPL Detroit Diesel 3–53. Timing delay/advance would then be characterized by comparing the injection timing parameters associated with biofuels with that of standard diesel legacy fuels. In addition the laser optical system would be configured to detect combustion, allowing for the ability to measure ignition delay. Figure 3 is a graphical representation of this, depicting a sample cylinder pressure versus crank angle curve along with specific events characterizing the injection process.

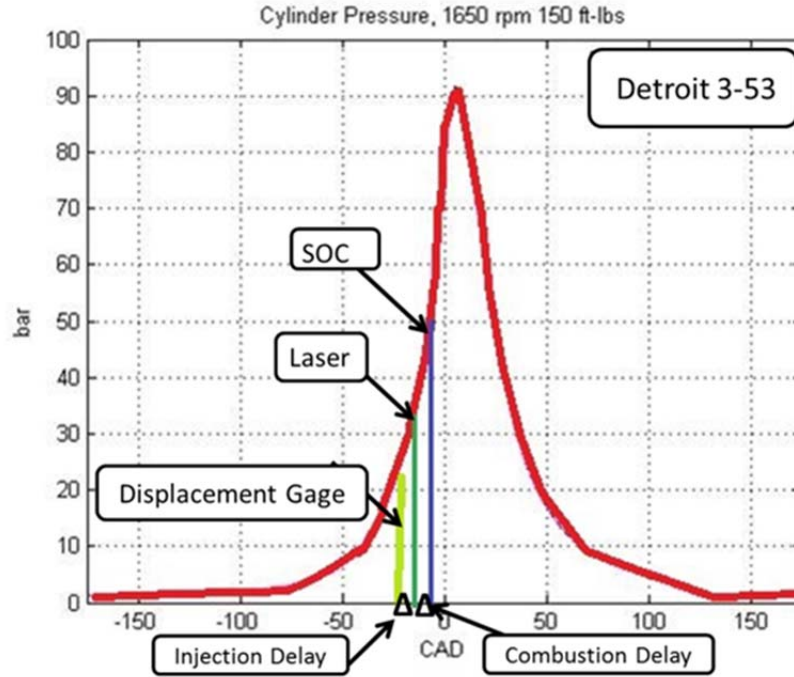


Figure 3. Sample cylinder pressure vs. CAD curve with an overlay of the injection and combustion delays.

B. LASER FLUORESCENCE

The measurement technique presented in this study relies on the use of laser induced fluorescence (LIF) to detect the presence of a dye-seeded fuel spray. LIF is often used to detect the fluorescent signal generated by an organic dye for the purpose of flow visualization and other measurements. Typically, an excitation wavelength is selected to be sufficiently separated from the fluorescence wavelength of the species of interest. The incoming laser excites the electrons of the target species to a higher energy level. After a period of time known as the fluorescence lifetime, the electrons de-excite and emit light at a longer wave length than the original excitation wavelength [30]. Figure 4 is a graphical representation of this process. Further details are available in [30].

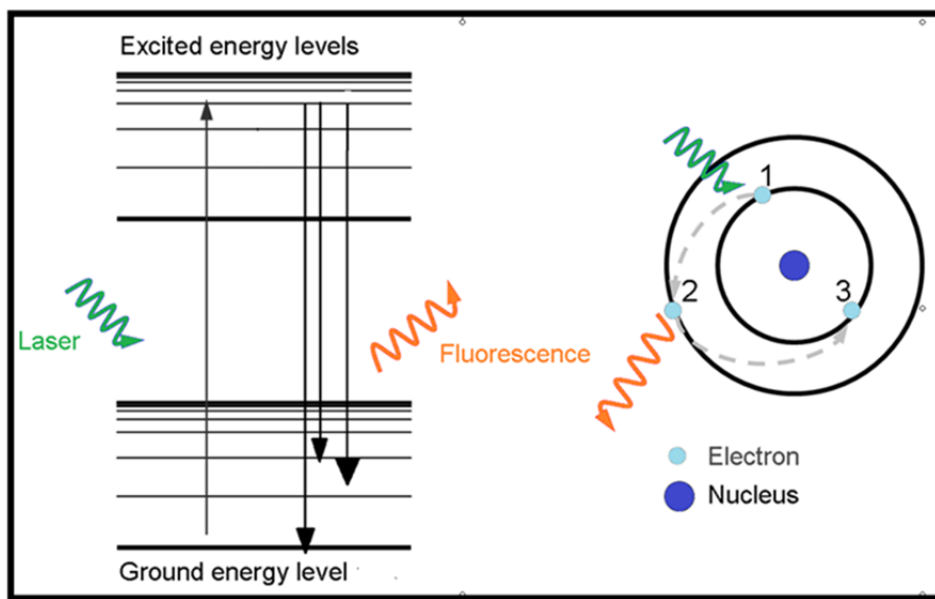


Figure 4. A graphical representation of laser induced fluorescence, showing an excitation wave length in green and the fluorescent response at a lower, orange, wave length, after [31].

A diode pumped, 100 mW, solid state, 532 nm, laser powered by an in house built power supply is used to excite pyrromethene 597 (Exciton Corporation of Dayton, Ohio) dissolved in the diesel fuel and its blends with HRD and SPK. Figure 5 is a sample absorption and emissions spectra provided by Exciton, for pyrromethene dissolved in gasoline. The manufacturer currently does not have specific spectra for diesel fuel, or F-76 available, but states that a similar single modal response can be expected with a similar peak absorption wavelength ($\lambda_{A \max}$) and peak fluorescence wavelengths ($\lambda_{F \max}$). Figure 6 is a similar curve from a 2004 study by Prieto et al. [32] showing the behavior of pyrromethene 597 in isooctane and 2,2,2-triflouroethanol.

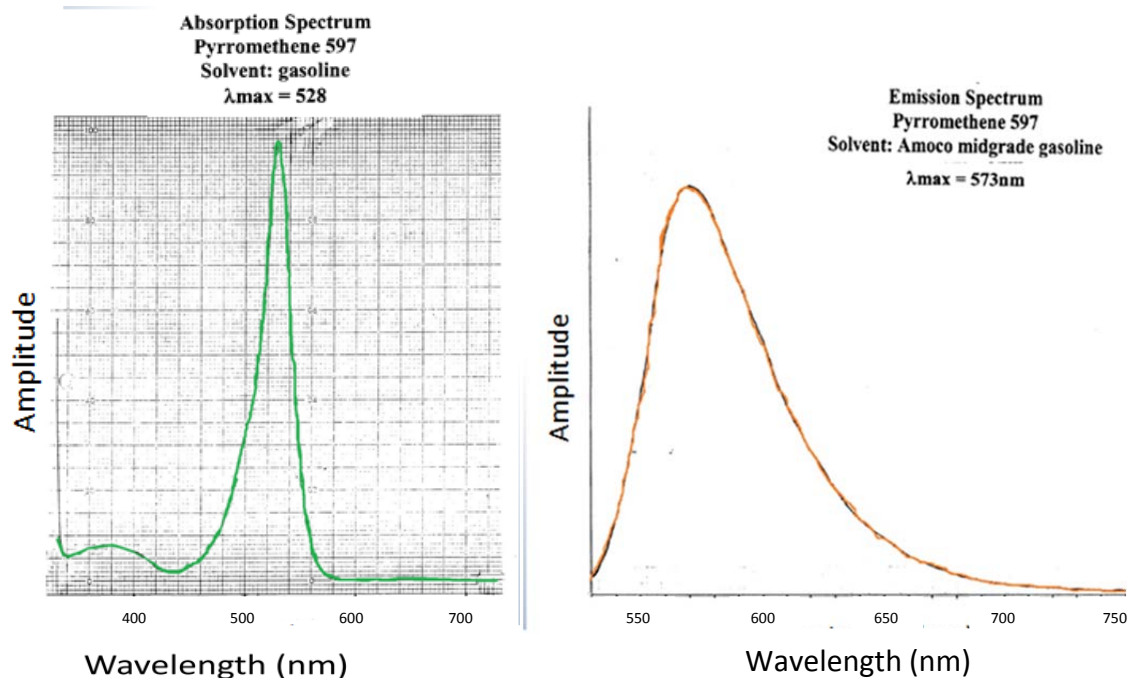


Figure 5. Absorption and emissions spectra for pyrromethene 597 dissolved in gasoline, after [33].

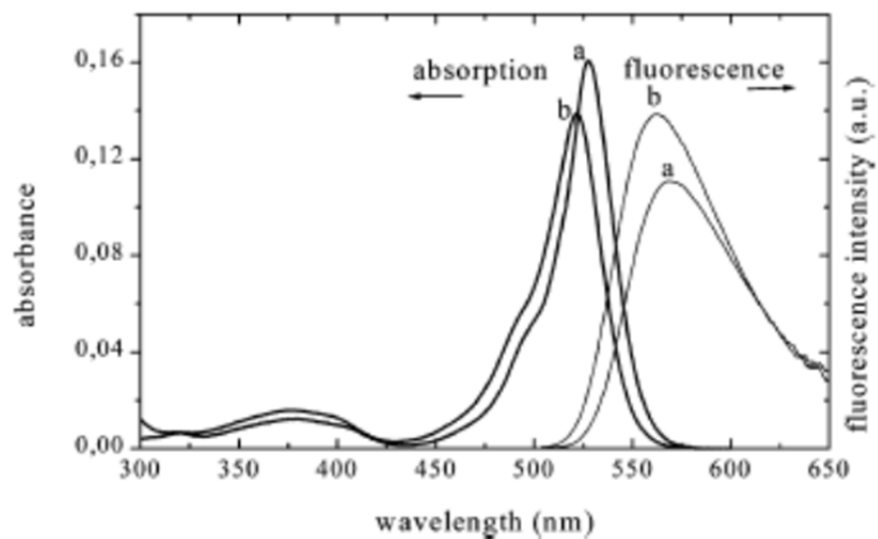


Figure 6. Absorption (bold lines) and fluorescence (thin lines) spectra of pyrromethene 597 at 2×10^{-6} M in isooctane (a) and 2,2,2-trifluoroethanol (b). Intensity is normalized to the fluorescence quantum yield, from [32].

Prieto et al. [32] studied the response of pyrromethene 597 dissolved in 22 different solvents to excitation at 495 nm. They reported $\lambda_{A \text{ max}}$ of 520.8 to 529.0 nm and $\lambda_{F \text{ max}}$ ranging from 560.6 to 571.2 nm. The fluorescence lifetime varies from 3.91 to 4.69 ns. In correlating this data to that provided by Exciton [33,34], the only common solvent is ethanol, for which both sources report the same $\lambda_{A \text{ max}}$, but the $\lambda_{F \text{ max}}$ reported by the manufacturer is 6 nm less than that reported by Prieto [32]. This may be due to differences in concentrations tested as Prieto reports that high dye concentrations shift the fluorescence band to lower energies [32]. The data all show a similar single modal response with an expected Stokes shift from 37.7–41.9 nm. Since the fuels being excited in this study are a blend of multiple components rather than pure solvents, a wider variance in the fluorescence curve than is shown in Figures 5 and 6 is expected. Figure 7 is a photograph taken during bench-top testing, and shows both the laser excitation and the responding fluorescence.

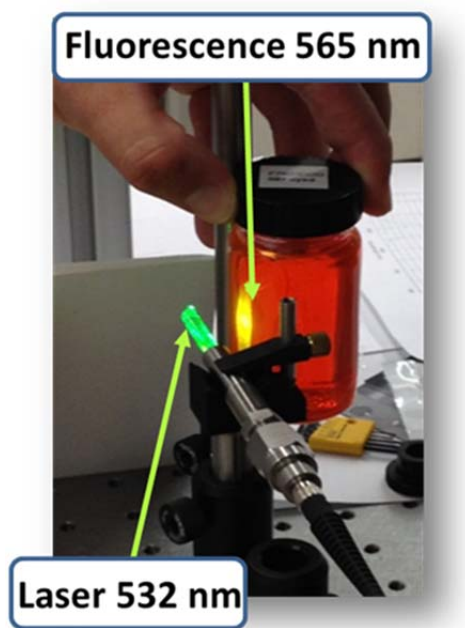


Figure 7. The 532 nm laser exciting a response from F-76 seeded with pyrromethene 597.

C. EXPERIMENTAL SETUP

A schematic view of the relative positioning of the fuel injector, displacement sensor, and laser sapphire rod is shown in Figure 8. A single sapphire rod, mounted in the glow plug port of the MPL's Detroit Diesel 3-53 serves as both the transmitting and receiving path for the laser signal [35]. The 532 nm excitation wavelength generates a fluorescence response from the pyromethene seeded fuel spray, which is recorded by the data acquisition system. The time differential between the displacement sensor signal indicating sealing of the injector chamber, and the laser fluorescence signal indicating a fuel spray in the cylinder, can be correlated to CA degrees and will serve to bracket the injection event. Figure 9 is a schematic of the complete experimental set-up, showing the relationship of the engine mounted sensors to the free-standing optics assembly, excitation laser, and signal processing oscilloscope and computer [35].

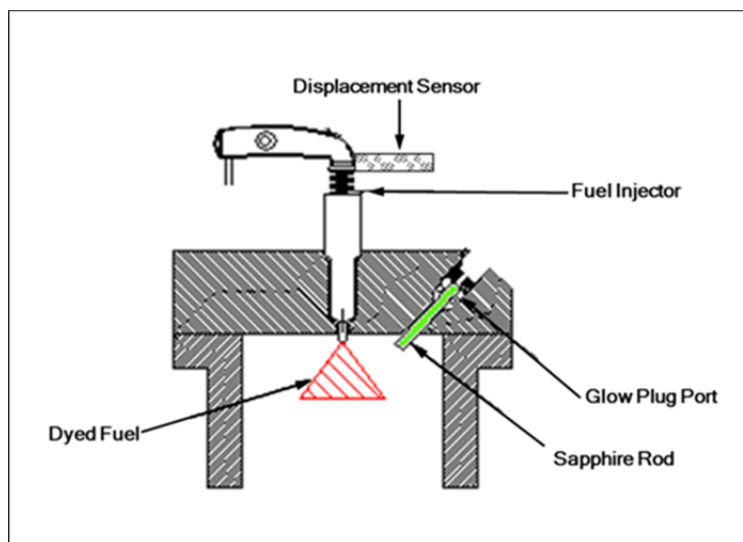


Figure 8. Schematic view of the displacement sensor, laser sapphire rod, and dyed fuel spray. after [35].

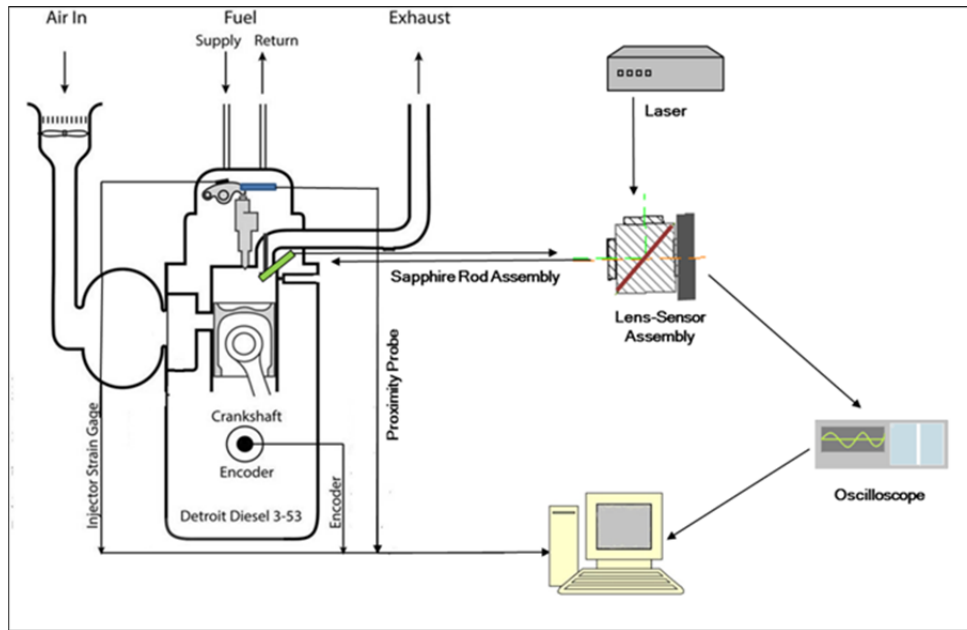


Figure 9. Schematic of the complete experimental set-up, showing the relationship of the engine mounted sensors to the free-standing optics assembly, signal generating laser, and signal processing oscilloscope and computer, after [35].

1. Engine

The engine used is a Detroit Diesel 3–53 currently located in the Marine Propulsion Laboratory at the Naval Postgraduate School. It is an in-line, direct injected, two-stroke engine that was used to power an Army semi-amphibious vehicle, the Gamma Goat. This particular variant of the 3–53 has glow plug ports, which were the key consideration in designing the configuration of the optical system. Table 4 lists key specifications for this engine.

Table 4. Specifications for Detroit Diesel 3–53 from [36].

Detroit Diesel 3–53 Specifications	
Model Number	5033–5001 N
Number of Cylinders	3
Bore and Stroke	9.84 x 11.43 cm (3.875 x 4.5 in.)
Engine Displacement	2605.5 cm ³ (159 in. ³)
Compression ratio	21:1
Maximum Power Output	101 hp at 2,800 rpm
Maximum Torque	278 N-m (205 ft-lbs) at 1,560 RPM
Brake mean Effective Pressure	669 kPa (97 lb/in. ²)

2. Displacement Sensor

The proximity probe used to detect the displacement of the top of the injector is model E2E-CR8C2, produced by Omron Corp. of Kyoto, Japan. It is a cylindrical, 4 mm diameter, pre-wired, oil resistant probe with a sensing distance of 0.8 mm. The sensor is designed to detect ferrous metal of a minimum size 5 mm x 5 mm x 1 mm, and has a response frequency of 3 kHz. Figure 10 and Figure 11 show sensing distance curves for this family of sensors. The complete data sheet can be found in Appendix A.

E2E-CR8

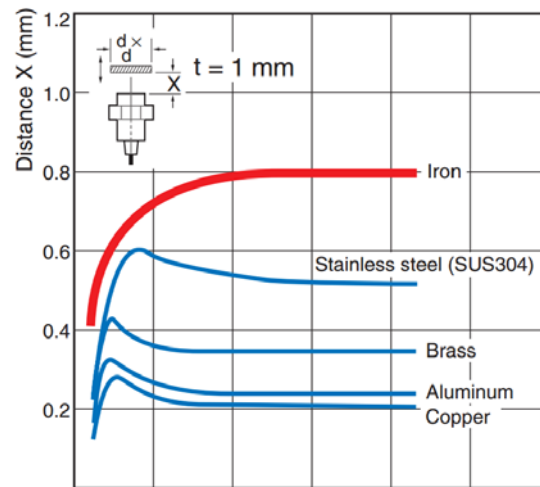


Figure 10. Side length sensing distance of E2E-CR8 family of sensors for various metals from [37]

E2E-C□C□/-X□C□

E2E-C□B1/-X□B□

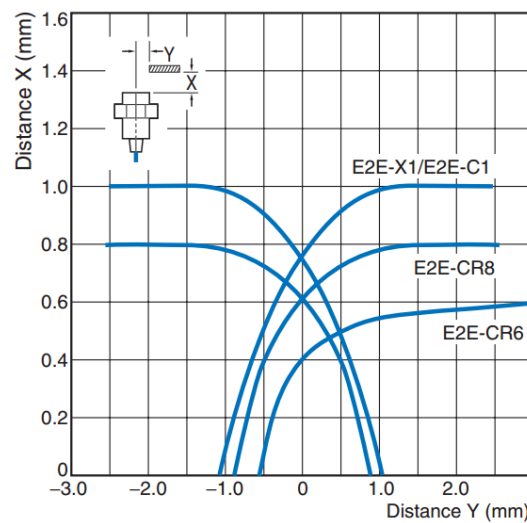


Figure 11. Off center displacement versus sensing distance for E2E-CR8 family of sensors from [37]

Figure 12 is a 3-D rendering, produced in Solidworks, of the bracket designed to hold the proximity probe in place. The bracket is designed to install on one of the rocker arm bracket bolts. A sensor holder, then positions the proximity probe .3620 cm (0.1425

in.) below the top of the injector. Figure 13 is a photograph of the installed bracket and mounted sensor. Detailed drawings are available in Appendix B.

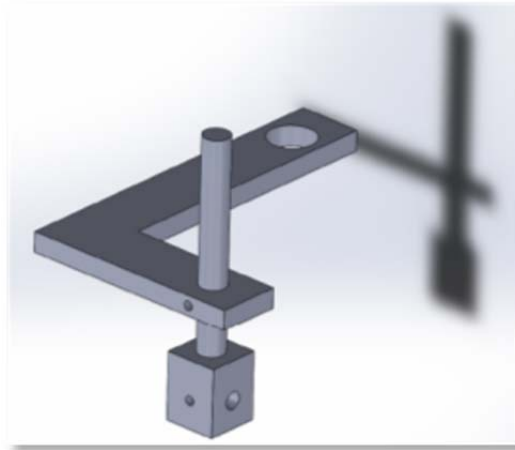


Figure 12. 3-D rendering, produced using Solidworks, of the complete mounting bracket for the proximity probe, courtesy of D. Seivwright.

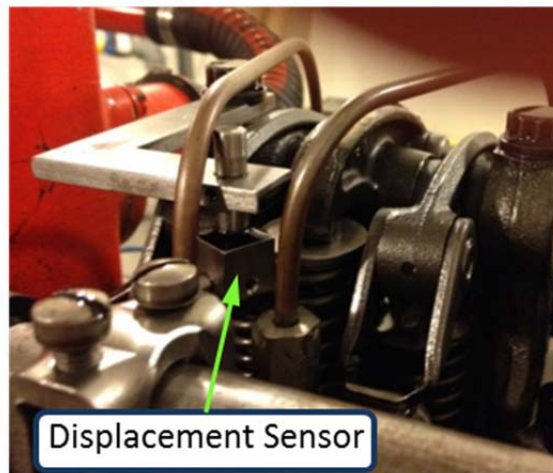


Figure 13. E2E-CR8C2 probe and mounting bracket installed on the head of the MPL's Detroit Diesel 3-53.

3. Sapphire Rod Assembly

The sapphire rod assembly consists of an external instrument bracket, an assembly tube, upper and lower rod housings, and the sapphire transmission rod.

a. Sapphire Rod

The sapphire rod was manufactured of HEM stock material by INASCO Corporation of Quakertown, PA. Dimensions and specifications of the sapphire transmission rod are shown in Table 5. A detailed drawing is available in Appendix C.

Table 5. Laser Transmission Rod Specifications from [37]

Laser Transmission Rod Specifications	
Length	10.16 cm (4 in.)
Diameter	0.20765 cm (0.1875 in.)
Hardness	9 Mohs
End Shape	45 deg. bevel
Transmissibility	85–87% (500–1000 nm)
Surface quality	60–40 scratch and dig
Smoothness	<20 Angstroms
Flatness	0.25 wave/inch
Crustal Orientation	0 degrees

b. Upper and Lower Rod Housings

The design of the upper and lower rod housings is loosely based on a similar fitting produced by Swagelok of Solon, OH. Figure 14 is a photograph of the upper and lower rod housings, polytetrafluoroethylene (PTFE) ferrules, and one collimator lens.



Figure 14. Sapphire rod, upper and lower rod housings with PTFE ferrules, and collimator lens.

The lower housing is 5.08 cm (2.0 in.) long with a 0.476 cm (3/16 in.) bore. The lower set of threads (M10 x 1.0 RH) mates to the engine glow plug port. The upper set of threads (3/8 x 24 UNF RH) mates to the upper rod housing. Between the two sets of threads is a 1.111 cm (7/16 in.) hex fitting, to allow the assembly to be firmly screwed into the glow plug port. Between the upper and lower housings is a set of 0.476 cm (3/16 in.) PTFE ferrules (Swagelok part number T-303-1 and T-304-1). The ferrules serve to make a firm pressure tight seal around the sapphire rod to prevent combustion gases from escaping. PTFE was used in place of steel for flexibility to account for the different coefficients of expansion of the rod and housing while providing for a proper seal throughout the operating temperature range of the engine. The upper housing has a 1.429 cm (9/16 in.) hex fitting to allow it to be tightened onto the lower housing. The top of the upper housing is bored out to a width of 1.050 cm (0.4133 in.) and a depth of 0.399 cm (0.157 in.), and threaded (M11 x 0.5) allow the attachment of a collimator lens. The fitting has a straight through bore of 0.389 cm (0.153 in.) to allow the passage of light from the collimator lens to the sapphire rod. Detailed drawings are available in Appendices D and E.

c. Assembly Sleeve

The assembly sleeve is 9.784 cm (3.852 in.) long with a 1.895 cm (0.746 in.) outer diameter. It is bored to an internal diameter of 1.50 cm (0.59 in.) for 5.641 cm (2.221 in.) and an internal diameter of 0.652 in for a length of 1.631 in. At the wider end there is a 0.089 cm (0.035 in.) chamfer that matches the interior of the glow plug port. Figure 15 shows the complete sapphire rod assembly, with the sleeve sitting over the upper housing.



Figure 15. Complete sapphire rod assembly, sapphire rod and lower housing protruding from the sleeve.

The purpose of the sleeve is to both prevent abrasion between the fiber optic cable and the rough cast interior of the glow plug port and to transmit a positive force to the top to the upper rod housing, preventing the sapphire rod and rod housing from shifting due to changing pressures in the cylinder. Figure 16 is a 3-D section view, produced in Solidworks, of the complete sapphire rod assembly. Detailed drawings are available in Appendix F.

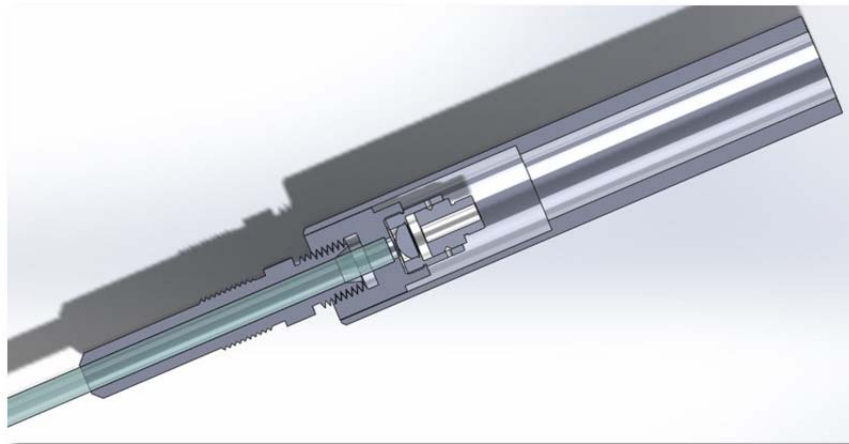


Figure 16. Section view of the complete sapphire rod assembly showing the rod, upper and lower housings and the sleeve.

4. External Instrument Bracket

The external instrument bracket is designed to mount to the exhaust manifold of the Detroit Diesel 3-53 engine and secure the sapphire rod assembly. The bracket bolts to

the exhaust manifold through two purpose added bosses, and clamps around the top of the sapphire rod assembly tube. The bracket, as shown in Figure 17, is designed to fit over a previously existing boss that had been used to mount an exhaust temperature sensor.



Figure 17. External instrument bracket shown mounted to a Detroit Diesel 3–53 exhaust manifold.

The top of the bracket is angled 47° from the horizontal to match the incline of the glow plug port. The 1.91 cm (0.75 in.) clamp is secured with #8–32 size screw. The clamping force is sufficient to prevent any motion of the tube and therefore the entire sapphire rod assembly. Figure 18 shows the instrument bracket mounted on the engine in addition to a section view of the complete assembly as seen from the left side of the engine. Also of note in the section view is the location of the engine seal, the threads on the lower housing of the sapphire rod assembly mate to threads within the glow plug port. Detailed drawings are available in Appendix G.

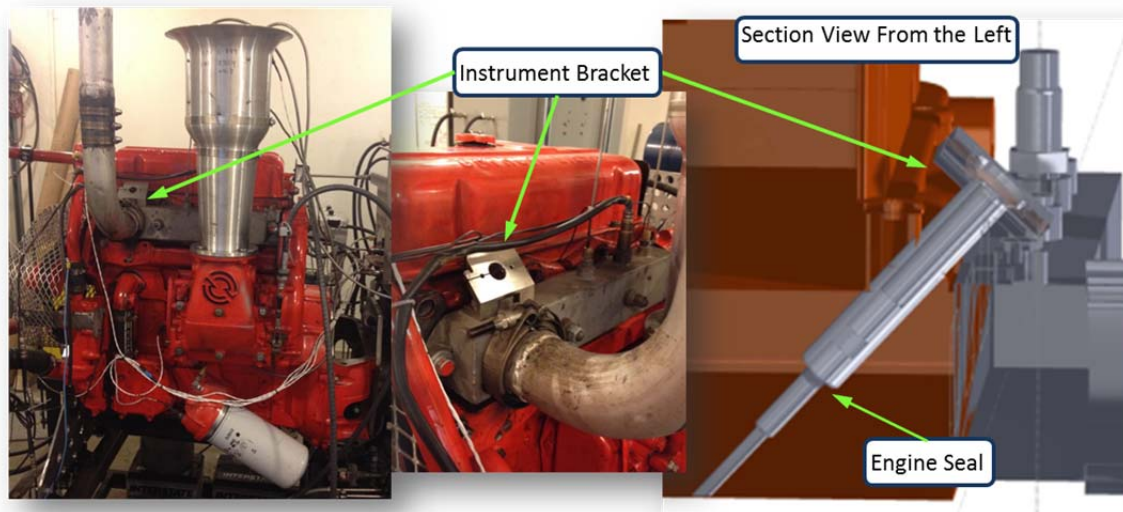


Figure 18. Photos of the instrument bracket mounted to the Detroit Diesel 3–53 and section view, produced in Solidworks, from the left side showing the complete sapphire rod assembly mounted in the engine.

5. Laser

The excitation laser used in this set-up is 532 nm, diode pumped, 100 mW, solid state laser with an in house built power supply. The laser was manufactured by Elforlight Ltd. of Daventry, UK. Specifications are shown in Table 5.

Table 6. Specifications for Laser from [35]

Model	Elforlight G4+100
Wavelength	532 +/- nm
Energy	100 mW
Polarization	Vertical (s)
Noise	< 0.5% RMS (typ 0.2%)
Divergence	<1mRad

6. Lens-Sensor Assembly

The parts of the lens-sensor assembly are all mounted a CM1 series cage-cube, produced by Thorlabs Inc. of Newton, New Jersey. The cage-cube contains an integrated filter mount capable of holding a rectangular lens 25 mm x 36 mm and up to 3 mm thick,

at a 45° angle to an incoming light beam. It also allows for the attachment of up to four external components. Figure 19 is a catalog image of a cage-cube and integrated filter mount. The left image in Figure 20 is a photo of the complete lens sensor assembly with green arrows indicating the path of the 532 nm excitation signal and orange arrows indicating the path of the response. The right image is a section view of the same assembly produced in Solidworks, illustrating the internal light path.



Figure 19. Catalog image of a CM1 series cage-cube from [36].

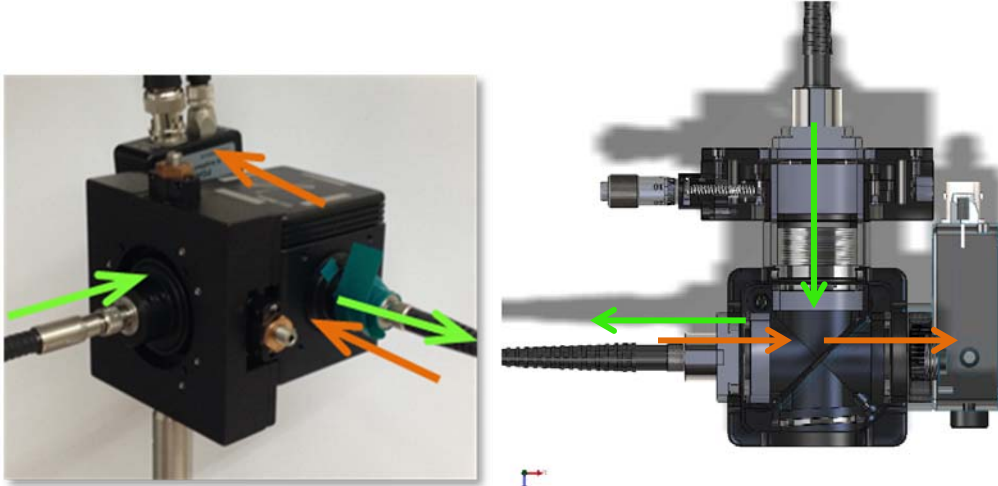


Figure 20. External photo of the complete lens-sensor assembly, green arrows indicate excitation signal, orange arrows indicate the response signal, and a section view of the same assembly produced in Solidworks, illustrating the internal light path.

a. Dichroic Mirror

The dichroic mirror is model DMLP567R, manufactured Thorlabs Inc. of Newton, New Jersey. It has cutoff wavelength of 567 nm, and a reflection band of 380–550 nm. For p-polarized light at 532 nm there is an expected transmission rate of up to 5.91 %, for the same wavelength polarized in the s plane the transmission is up to 0.15% [41]. Figure 21 shows the transmission and reflectance curves in response to s-polarized light.

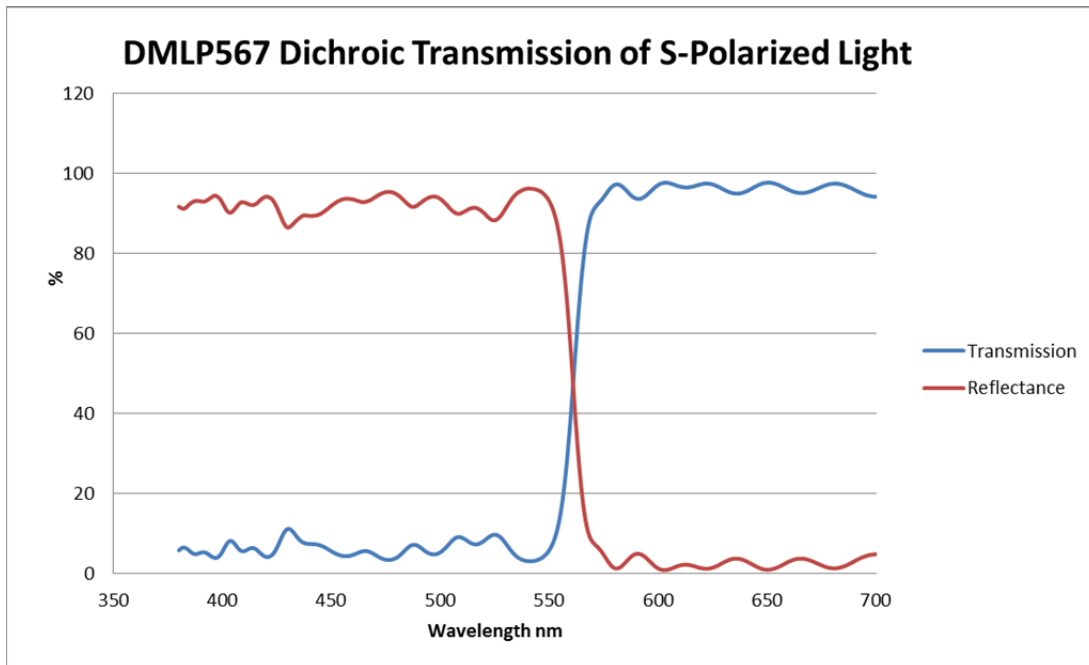


Figure 21. Transmission and reflectance for DMLP567 series dichroic filter in response to s-polarized light, after [41].

b. Sensor

The sensor used for this project is the PDA36A switchable gain photodetector produced by ThorLabs Inc. of Newton, New Jersey. It has a sensitivity range of 350–1100 nm and a 3.6 mm x 3.6 mm sensor. The responsivity curve is shown in Figure 22. The gain is adjustable in 8, 10 dB steps [42].

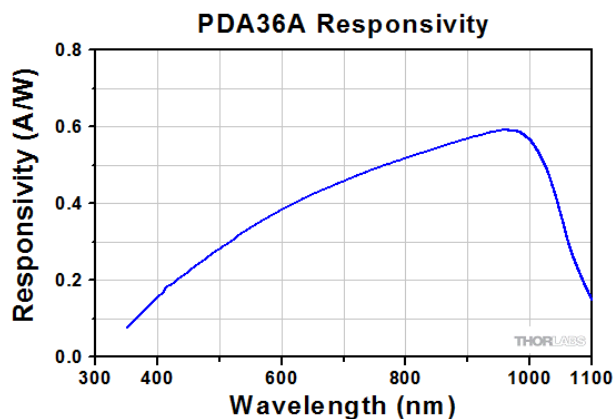


Figure 22. Response curve for PDA36A Switchable Gain Detector from [42].

c. Filter

The filter used between the dichroic mirror and the sensor, to filter out any 523 nm leakage, is part number FB590–10, obtained from Thorlabs Inc. of Newton, NJ. The transmission spectrum for this filter is shown, in Figure 23. The center frequency for this filter is 590 +/- 2 nm, and peak transmission is 56.58 %.

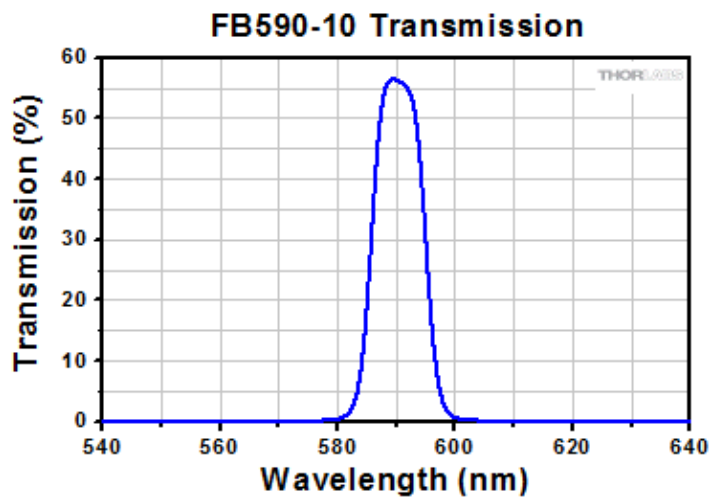


Figure 23. Transmission spectrum for FB590–10 dielectric filter from [43].

This lens was chosen based on data provided by Excition Corp. on the behavior of pyrromethene 597–8C9 in diesel fuel, which indicated a peak fluorescence at 590 nm.

The manufacturer indicated that pyrromethene 597, the dye used in this study, exhibits similar behavior, despite no data being available [33].

d. Fiber Optic Cables

Two types of fiber optic cable were used in this project, both procured from Thorlabs Inc. of Newton, New Jersey. To make the connection from the laser to the lens-sensor assembly, item number FT800UMT, a 0.39 numerical aperture (NA), 800 nm core, high-OH, multimode optical fiber with a wavelength range of 300–1,200 nm is used [44]. The attenuation curve for this fiber is show in blue in Figure 24.

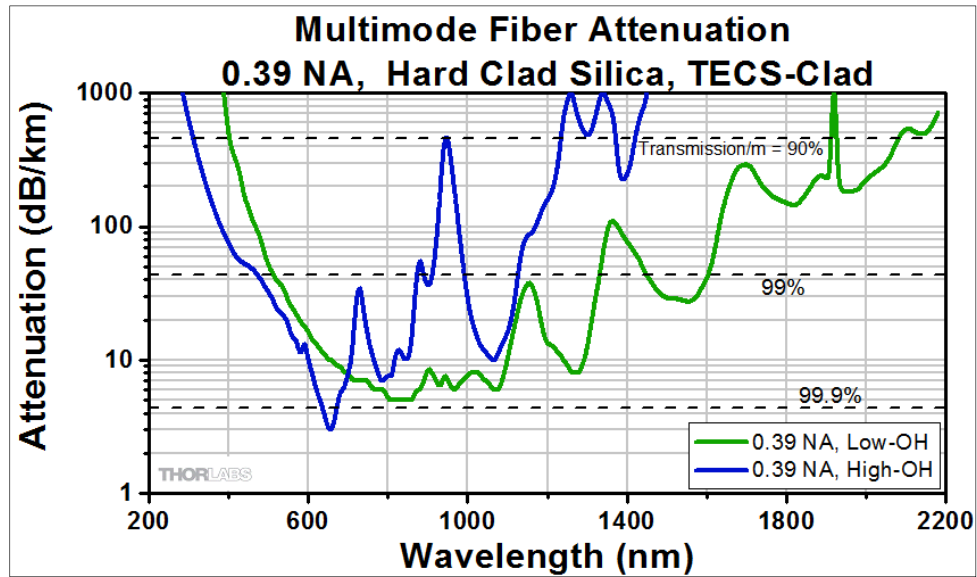


Figure 24. Attenuation curves for 0.39 NA, 800nm fiber optics from [44].

To connect the lens-sensor assembly to the sapphire rod assembly, item number M40L02, a 400 nm, 0.48 NA, low-OH fiber rated for 400–2200 nm is used [45]. The attenuation curve for this fiber is show in Figure 25.

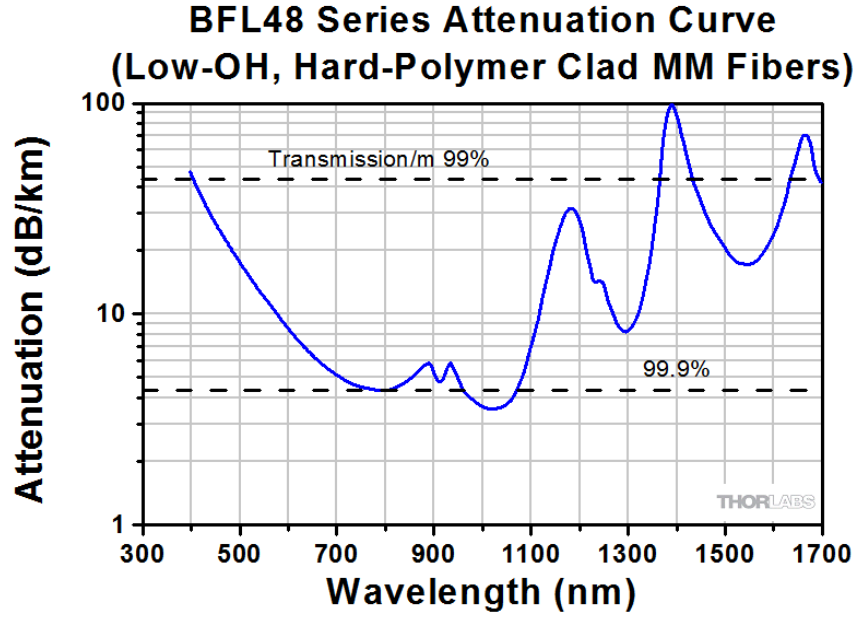


Figure 25. Attenuation curves for 0.48 NA, 400nm fiber optics from [45].

e. Collimation Lenses

Collimator lenses are used to narrow a beam or make the direction of motion more parallel. There are three collimators used in the set-up. The first is located at the junction where the laser light first enters the cage-cube. This collimator, part number F240SMA-A, procured from Thorlabs Inc. of Newton, New Jersey, has an 7.86 mm focal length and a numerical aperture of 0.5. It ensures that the laser beam hitting the dichroic mirror has relatively small cross section and remains focused. Prior to exiting the cage-cube the light passes through a second collimator, part number F280SMA-A, also procured from Thorlabs Inc. This lens has a much smaller numerical aperture of 0.15 and a 18.07 mm focal length. It serves to focus the light into the fiber optic cable leading to the sapphire rod assembly. At the junction of the second fiber optic cable and the sapphire rod assembly is a third collimator lens. This lens, part number F230SMA-A, also from Thorlabs Inc., has a numerical aperture of 0.57 and 4.34 mm focal length. This lens ensures that the laser beam is focused on the sapphire rod rather than the internal surfaces of the upper rod assembly. The catalog page with complete lens specifications can be found in Appendix H.

7. Oscilloscope

The oscilloscope used in designing and testing the set-up is a Hewlett-Packard 5460 B, manufactured by Hewlett-Packard of Palo Alto, CA. Signal sensitivity was set to the order of 5 mV.

THIS PAGE INTENTIONALLY LEFT BLANK

IV. DESIGN SPECIFICATIONS AND CHALLENGES

A. DESIGN CONSTRAINTS

The instrumentation designed for this project had to meet the following specifications:

- Mount on MPL's Detroit Diesel 3–53 without any significant permanent modifications to the engine.
- Operate in an environment that includes the high temperatures and vibrations seen on an operating two-stroke diesel engine.
- Allow the unimpeded operation of the engine

B. INITIAL DESIGN AND CHALLENGES

An operating diesel engine, with its high temperatures and vibrations, is a challenging environment for alignment sensitive optical equipment. The original design for this project, shown as a 3-D Solidworks model in Figure 26, included mounting the optical instrumentation on the instrument bracket. This posed concerns with vibrations and transmission of heat from the exhaust manifold to the lens-sensor assembly. An attempt was made to mitigate the amount of heat transferred to the optics assembly from the exhaust manifold and instrument bracket by using 0.63 (0.25 in.) thick PTFE spacer between the metal surface of the instrument bracket and the cage-cube of the optics assembly.

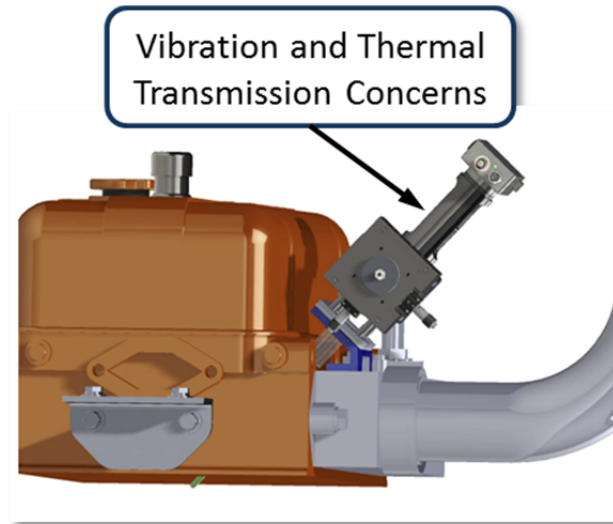


Figure 26. Solidworks model of original design showing optics mounted on the instrument bracket.

Other issues included the need to ensure clearance between the piston at top-dead-center (TDC) and the sapphire rod while providing sufficient line-of-sight of the injector nozzle, and to provide a pressure tight seal in the glow plug port. The seal must also constrain any movement of the brittle sapphire rod, which could shatter from an impact induced by the pressure changes within the cylinder. Figure 27 is a section view of the cylinder head, rendered in Solidworks, showing the location of the sealing point between the sapphire rod assembly and the engine. It also illustrates the sapphire rod protruding from the cylinder head, and thus and the need to ensure sufficient clearance when the piston is at TDC.

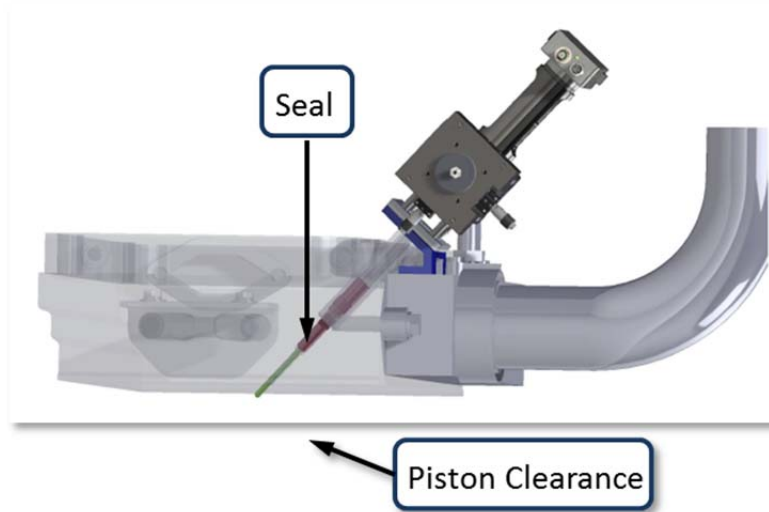


Figure 27. Section view of the cylinder head with the location of the engine seal and the need to ensure adequate clearance between the piston and the sapphire rod at TDC highlighted.

A further difficulty was encountered in designing the instrument bracket. The need to mount it securely to the engine, in combination with the need to hold the assembly tube tightly against the variations in cylinder pressure and the small clearance between the existing boss on the exhaust manifold and the cylinder head all drove the final design toward the shape shown. An initial version of the part was proposed as being made of two separate pieces that were to be welded together, and then welded to the assembly tube, however the distortion caused by the heat from welding made this an impractical fabrication method. The final result, with a clamping mechanism holding the assembly tube in place, was inspired by a bicycle seat clamp, but still resulted in some fabrication difficulties. The undercut highlighted in Figure 28 was at the limit of the Mechanical and Aerospace Engineering Department's CNC machine. A second set of issues, also highlighted in Figure 28, only became apparent upon receipt of the original sapphire rod and assembly of the system. The original design included transmission of both the excitation and fluorescence signals through an air gap of approximately 10.4 cm (4.1 in.) This resulted in the excitation signal becoming too diffuse to effectively transmit down the sapphire rod.

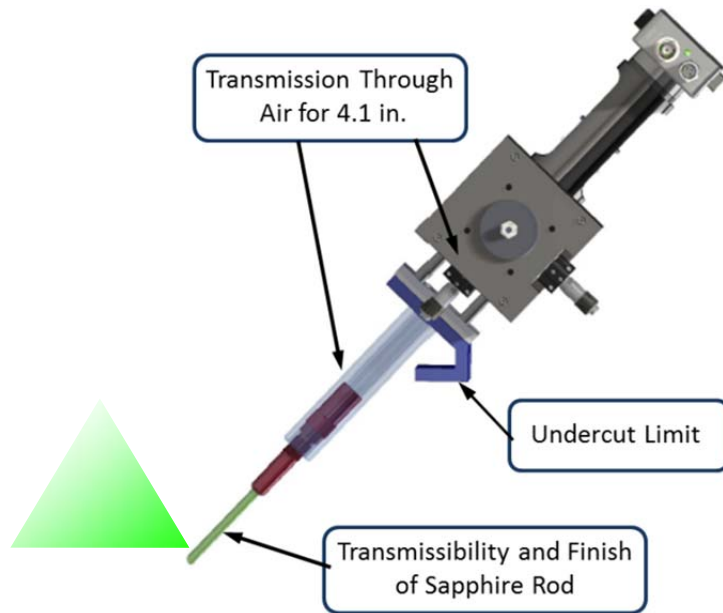


Figure 28. The original design iteration included a large air gap, welded fabrication of the instrument bracket, and a sapphire rod of low quality material.

In resolving the issue of the decollimated signal, by using fiber optic cable and a pair of collimating lenses to couple the cage-cube with the sapphire rod, the problem of mitigating the heat and vibration of a running engine was also resolved. This design change allowed the lens-sensor assembly to be removed from the instrument bracket and instead mounted on a stable room-temperature surface, such as work bench. Also included as a design consideration, is the transmissibility and end finish on the sapphire rod. The original sapphire rods procured for this project had several different end finishes, but were of poor quality material and did not transmit the excitation and fluorescence signals well enough to generate a data response. Due to various time and budget constraints, a single replacement was ordered, in a much higher quality material and with a 45° angled end. This results in the signals transmitting and receiving through the curved sides of the rod, with the end face acting as a mirror. A more optimal configuration would be a rounded end, which would allow the use of all exposed surface area as a transmitting and receiving medium.

IV. RESULTS AND DISCUSSION

During initial bench-top testing, the system produced a response of 3 mV on the oscilloscope. This response is produced by holding a jar of dyed fuel adjacent to the sapphire rod. A response of approximately 5 mV was seen when holding a fuel soaked strip of office paper directly against the sapphire rod. Figure 29 contains photographs of the back of the lens-sensor assembly with the sensor removed; the image on the left shows signal return with a jar of dyed fuel being held against the sapphire rod, the image on the right shows the filtered signal without any fluorescence present.



Figure 29. The left image show the fluorescence response from a jar of fuel reaching the sensor, the right image shows no response reaching the sensor when the fuel is moved away.

Unfortunately, the signal reaching the sensor also contained a significant amount of 532 nm light, making the sensor readings noisy and the fluorescence response difficult to detect, and requiring the use of a filter. Figure 30 is a photograph of the unfiltered signal reaching the sensor through the dichroic mirror. The visible green light is 532 nm leakage through the dichroic mirror. The center area that is slightly blue is a mixing of yellow fluorescence response and the 532 nm excitation wavelength. It is suspected that due to the s-polarization of the laser, the dichroic mirror is leaking up to 6 % of the 532 nm signal, however there are also several other possible causes for the light leakage.

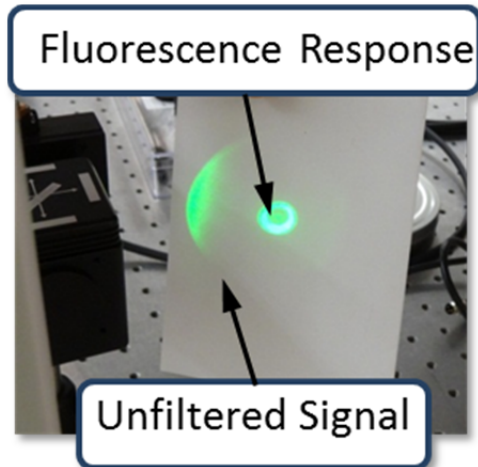


Figure 30. Unfiltered signal reaching the sensor though the dichroic mirror, a large amount of green 532 nm leakage is shown, with the bluish center portion being the mingling of the yellow fluorescence signal and the leakage.

The halo surrounding the signal is indicative of a numerical aperture mismatch somewhere in the system. Figure 31 is a sketch, produced using TurboCAD and Microsoft Paint, illustrating what happens when there is a numerical aperture mismatch in an optical junction. If the numerical aperture on the transmitting side is greater than that on the receiving side, the beam of light has divergence greater than the receiving optic it is being aimed at can accept. Not only will some of the signal not travel down the fiber, but it may also reflect back through the system.

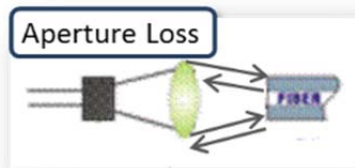


Figure 31. Numerical aperture loss, if the aperture on the sending side is greater than the aperture on the receiving side, some signal may reflect back through the system.

A numerical aperture mismatch is possible even between two identical pieces of fiber optic cable. In this case, it is suspected that the problem is at the junction between

the cage-cube and the fiber optic cable leading to the sapphire rod assembly. This same junction had been the source of some broadband light leakage that was corrected through the use of electrical tape.

A preliminary attempt was made to refine this setup and improve the clarity of the fluorescence signal by using a spectrometer, which became available toward the end of this project, to analyze both the excitation wavelength and the response. The HR 2000 spectrometer, manufactured by Ocean Optics Inc. of Dunedin, FL, uses a Sony ILX511B linear silicon CCD array and has a detector range of 200–1100 nm. A complete list of specifications can be found in Appendix I and Appendix J.

The output spectrum of the Elforlight G4+100 laser is shown in Figure 32. The laser output was measured without the use of a neutral density filter to modulate intensity. Instead, the beam was angled away from the spectrometer sensor slightly, until the spectrometer was no longer overloaded. The output ranges between 527.7–533.19 nm and peaks at 529.55 nm. This range of approximately 5.5 nm is not unusual for a diode pumped laser, and may be a contributing factor in the large amount of light leaking through the dichroic mirror. Any filter chosen to block the excitation wavelengths from the sensor must either be a notch filter with a large enough bandwidth to cover the full excitation spectrum or a bandpass filter does not impede the collection of any of the fluorescence signal.

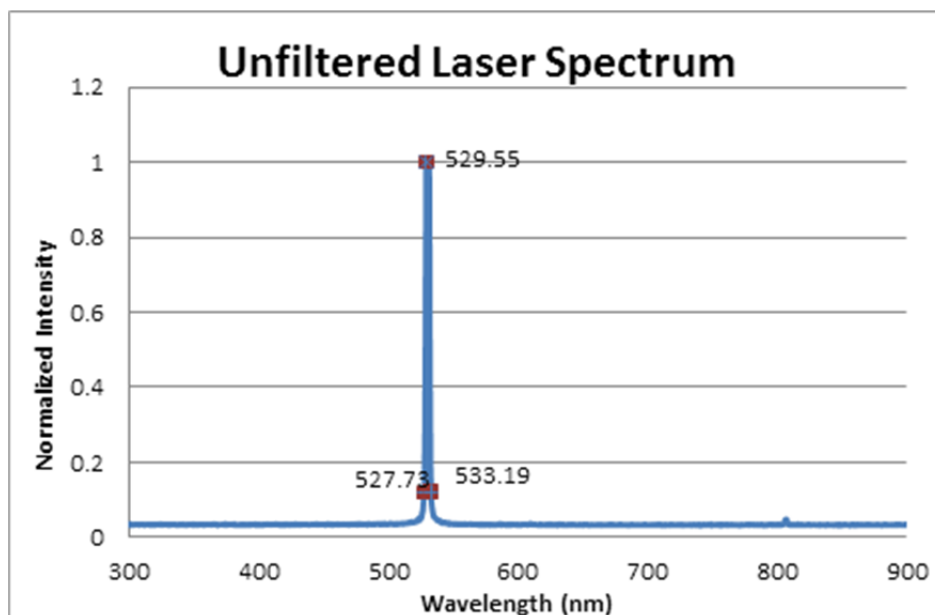


Figure 32. The unfiltered laser spectrum as measured by HR 2000 spectrometer under ambient laboratory lighting conditions.

The fluorescence spectrum for pyrromethene 597 dissolved in F-76 was captured by holding a fiber optic cable from the laser directly over a jar of dyed fuel and holding the spectrometer sensor cable at a slight angle to the surface of the fuel as it fluoresced. This was done to avoid any diffraction caused by the glass jar, and to avoid detecting the excitation wavelengths in addition to the fluorescence. The resulting spectrum is shown in Figure 33. The fluorescence response of pyrromethene 597 dissolved in F-76 has a range of 537.29–638.52 nm with a peak response at 568.16 nm. This peak response is in line with the data reported by Prieto et al. [32] for various pure solvents.

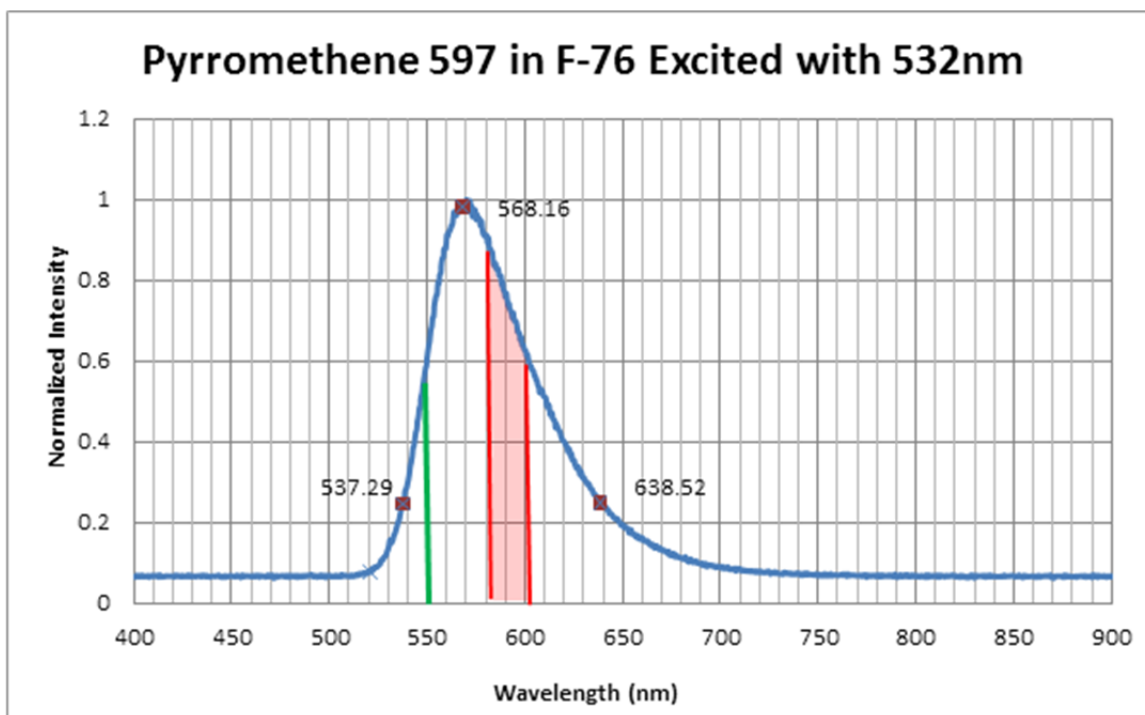


Figure 33. Spectrum of Pyrromethene 597 dissolved in F-76 as measured HR 2000 spectrometer under ambient laboratory lighting conditions. The red shaded area indicates the portion of spectrum visible to the sensor in the current set-up; the green line indicates the new cutoff resulting from the suggested refinements.

Both the dichroic mirror and the bandpass filter currently used in this experimental design block a significant portion of the response spectrum. The dichroic has a center wavelength at 567 nm, and the bandpass filter has a narrow band of 580–600 nm. The red shaded area overlaid on Figure 33 shows the portion of the fluorescence spectrum currently visible to the sensor. Using Simpson's Rule to integrate the raw data, this amounts to approximately 12.3% of the total response spectrum. A significant improvement in fluorescence signal strength is likely to be seen by using a dichroic mirror with a center wavelength at 550 nm and either a notch filter centered at 533 nm or an edgepass filter with a cutoff in the vicinity of 550 nm. Dielectric filters specifically designed for fluorescence imaging should also be considered, if one with the appropriate transmission range is available, since they often have a much higher transmissibility in their specified range than other filter types. The green line overlaid on Figure 33 shows the anticipated cut-off for the detectable spectrum. With the new suggested configuration,

approximately 76% of the fluorescence spectrum will be visible to the sensor. The increase in total fluorescence response reaching the sensor should compensate for the leakage of the excitation wavelengths and provide a useable data signal.

Despite the narrow band of fluorescence reaching the sensor in the current set-up, a detectable change in the oscilloscope readings in response the presence of dyed fuel can be seen. Further, this demonstrates that using a single transmitting and receiving port is a viable means to detect the presence of dyed fuel. With refinement in the choice of optical filters, a more robust and defined signal is anticipated, moving this technique beyond the bench-top testing phase.

V. CONCLUSIONS AND OBSERVATIONS

This project demonstrated that using a single receiving/transmitting port to detect an optical signal is a viable method for determining the timing of fuel entry into the combustion cylinder of an operational diesel engine. The technique presented is geared for engines with a readily accessible glow plug port and requires no modification of the engine block or cylinder head.

Although the prototype system has not been extensively tested for detecting combustion, the system readily propagates a significant broadband light signal to the sensor as demonstrated by using both a small incandescent flashlight and a handheld lighter. With the refinements suggested in the previous section, specifically targeting the 532 nm excitation frequency for filtration and allowing a significant portion of the visible spectrum to reach the sensor, it is anticipated that the system will be able to detect the combustion event within the engine cylinder. The actual initiation of combustion is typically measured by the 431.5 nm chemiluminescence of the carbon-hydrogen radical (CH^{*}). In this case, it is the visible and infrared portion of the signal that will be detected, allowing for a comparison of combustion timing between different fuels, but not the true start of combustion. To detect the 431.5 nm signal using this type of apparatus, significant re-design work is required.

This project has successfully designed, manufactured, and installed, a laser-based diagnostic assembly and instrument bracket, for detecting the presence of a dye seeded fuel spray in the combustion cylinder, on the Marine Propulsions Lab's Detroit Diesel 3-53. All custom-designed parts were produced to within tolerance and fit on the engine.

This project has also successfully modified the Marine Propulsion Lab's Detroit Diesel 3-53 for timing the start of injection using a proximity probe and the location of the injector head. The signal from the proximity probe has been correlated with the signal from the optical encoder, recording CA degrees, and the timing has been shown to be within expected tolerance. This data single coupled with the fluorescence and combustion

signals allows the timing of the initiation of injection, the entry of fuel into the combustion cylinder, and the initiation of combustion in crank angle degrees.

VI. FUTURE WORK

The instrumentation can be further refined to receive a more robust signal. This may include refining the choice of dichroic mirror and filter lens to better match the fluorescence spectrum, as well as investigating the use of a beam splitter to create a reference signal to subtract from the return. Also, various signal analysis methods will be investigated, including the use of a signal averaging program.

Once the optical instrumentation is refined to the point where a robust data signal is received, experiments can be run to characterize the time delay between start of injection, combustion, and fuel entry to the cylinder for F-76, HRD, SPK and their various blends. The data collected can then be used to determine if, and how, different fuel blends impact injection and combustion timing.

THIS PAGE INTENTIONALLY LEFT BLANK

APPENDIX A. E2E-CR8C2 DISPLACEMENT SENSOR SPECIFICATION

E2E

E2E-C□C/B□ and E2E-X1C/B□ DC 3-Wire Models

Size		3 dia.	4 dia.	M5	5.4 dia.
Shielded		Shielded			
Item	Model	E2E-CR6C/B□	E2E-CR8C/B□	E2E-X1C/B□	E2E-C1C/B□
Sensing distance		0.6 mm ±15%	0.8 mm ±15%	1 mm ±15%	
Set distance		0 to 0.4 mm	0 to 0.5 mm	0 to 0.7 mm	
Differential travel		15% max. of sensing distance			
Detectable object		Ferrous metal (The sensing distance decreases with non-ferrous metal. Refer to <i>Engineering Data</i> on pages 17 and 18.)			
Standard sensing object		Iron, 3 × 3 × 1 mm	Iron, 5 × 5 × 1 mm		
Response frequency *		2 kHz	3 kHz		
Power supply voltage (operating voltage range)		12 to 24 VDC (10 to 30 VDC), ripple (p-p): 10% max.			
Current consumption		10 mA max.	17 mA max.		
Control output	Load current	Open-collector output, 80 mA max. (30 VDC max.)	Open-collector output, 100 mA max. (30 VDC max.)		
	Residual voltage	1 V max. (Load current: 80 mA, Cable length: 2 m)	2 V max. (Load current: 100 mA, Cable length: 2 m)		
Indicators		Operation indicator (red)			
Operation mode (with sensing object approaching)		C1/B1 Models: NO Refer to the timing charts under <i>I/O Circuit Diagrams</i> on page 20 for details. C2 Models: NC			
Protection circuits		Reverse polarity protection, Surge suppressor			
Ambient temperature range		Operating/Storage: -25 to 70°C (with no icing or condensation)			
Ambient humidity range		Operating/Storage: 35% to 95% (with no condensation)			
Temperature influence		±15% max. of sensing distance at 23°C in the temperature range of -25 to 70°C			
Voltage influence		±5% max. of sensing distance at rated voltage in the rated voltage ±10% range	±2.5% max. of sensing distance at rated voltage in the rated voltage ±15% range		
Insulation resistance		50 MΩ min. (at 500 VDC) between current-carrying parts and case			
Dielectric strength		500 VAC, 50/60 Hz for 1 min between current-carrying parts and case			
Vibration resistance		Destruction: 10 to 55 Hz, 1.5-mm double amplitude for 2 hours each in X, Y, and Z directions			
Shock resistance		Destruction: 500 m/s ² 10 times each in X, Y, and Z directions			
Degree of protection		IEC 60529 IP66	IEC 60529 IP67, in-house standards: oil-resistant		
Connection method		Pre-wired Models (Standard cable length: 2 m)			
Weight (packed state)		Approx. 60 g			
Materials	Case	Stainless steel (SUS303)		Nickel-plated brass	
	Sensing surface	Heat-resistant ABS			
	Clamping nuts	Nickel-plated brass (E2E-X1C/B□ only)			
	Toothed washer	Zinc-plated iron (E2E-X1C/B□ only)			
Accessories		Instruction manual			

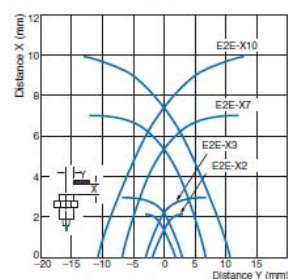
* The response frequency is an average value. Measurement conditions are as follows: standard sensing object, a distance of twice the standard sensing object, and a set distance of half the sensing distance.

Engineering Data (Reference Value)

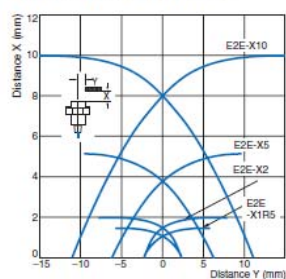
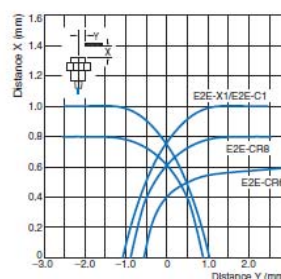
Sensing Area

Shielded Models

E2E-X□□□-X□□T1

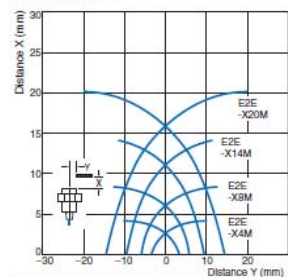


E2E-X□□□-X□□□-X□□□

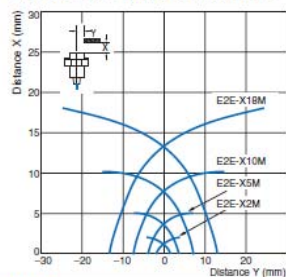
E2E-C□□□-X□□□
E2E-C□□B1/-X□□□

Unshielded Models

E2E-X□□MD□

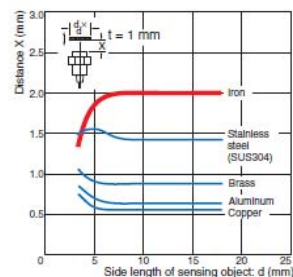


E2E-X□□ME□-X□□MY□-X□□MF□

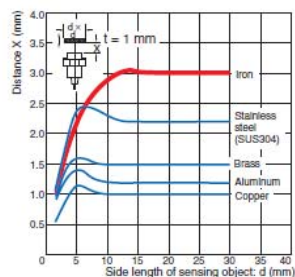


Influence of Sensing Object Size and Material

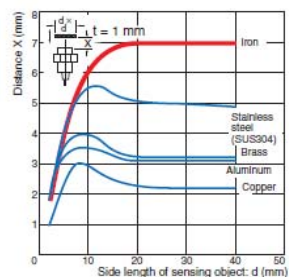
E2E-X2D□



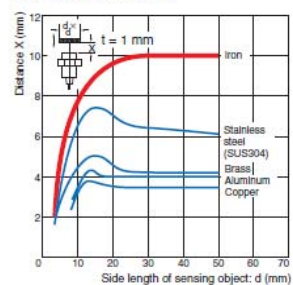
E2E-X3D□-X3T1



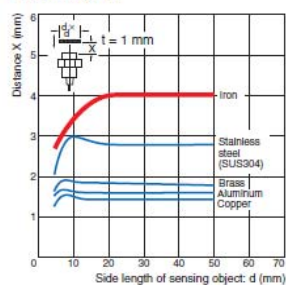
E2E-X7D□-X7T1



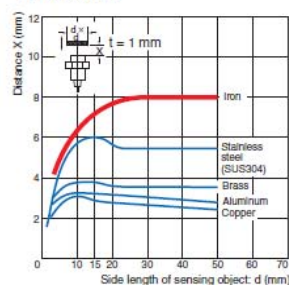
E2E-X10D□-X10T1



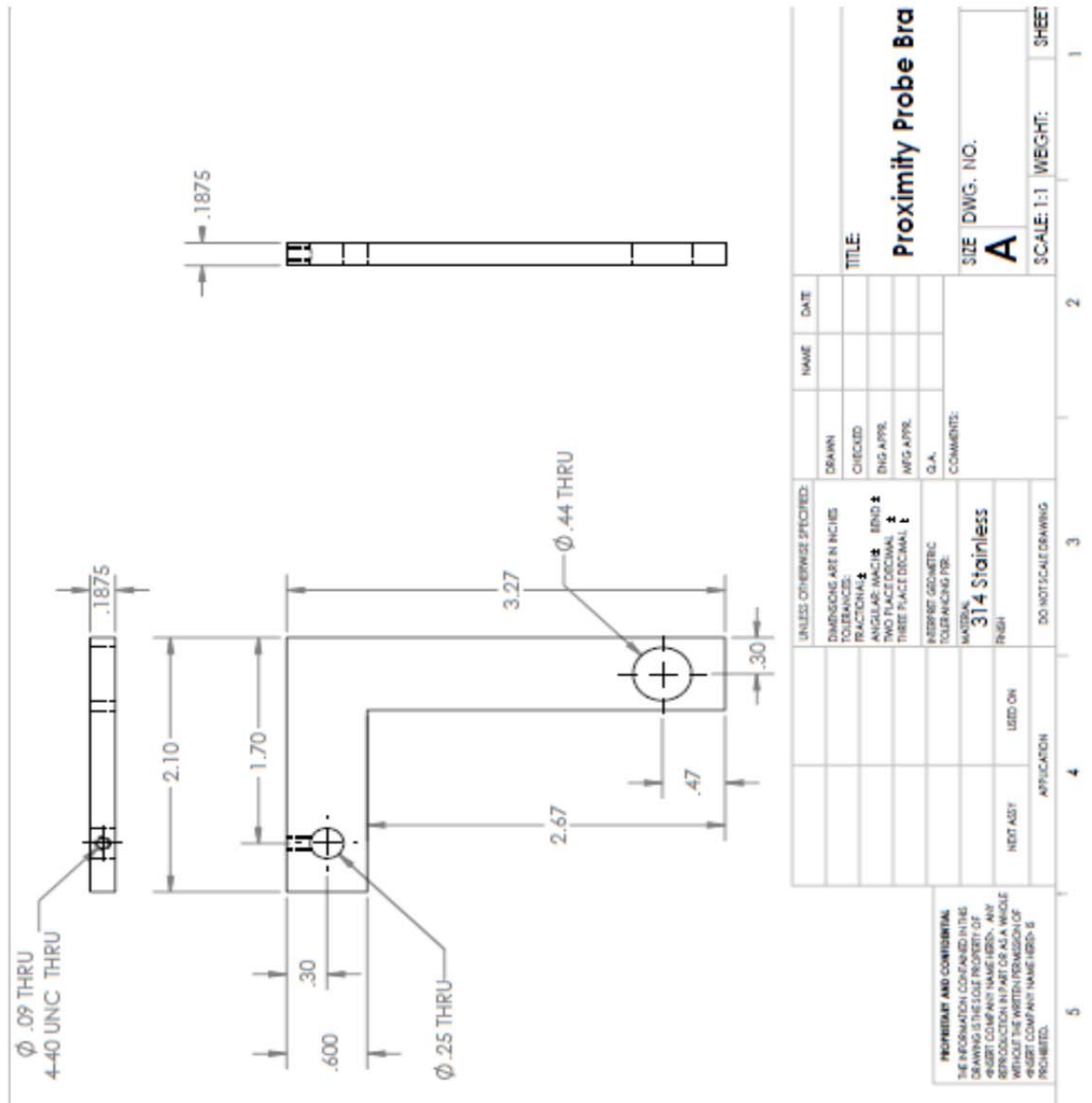
E2E-X4MD□

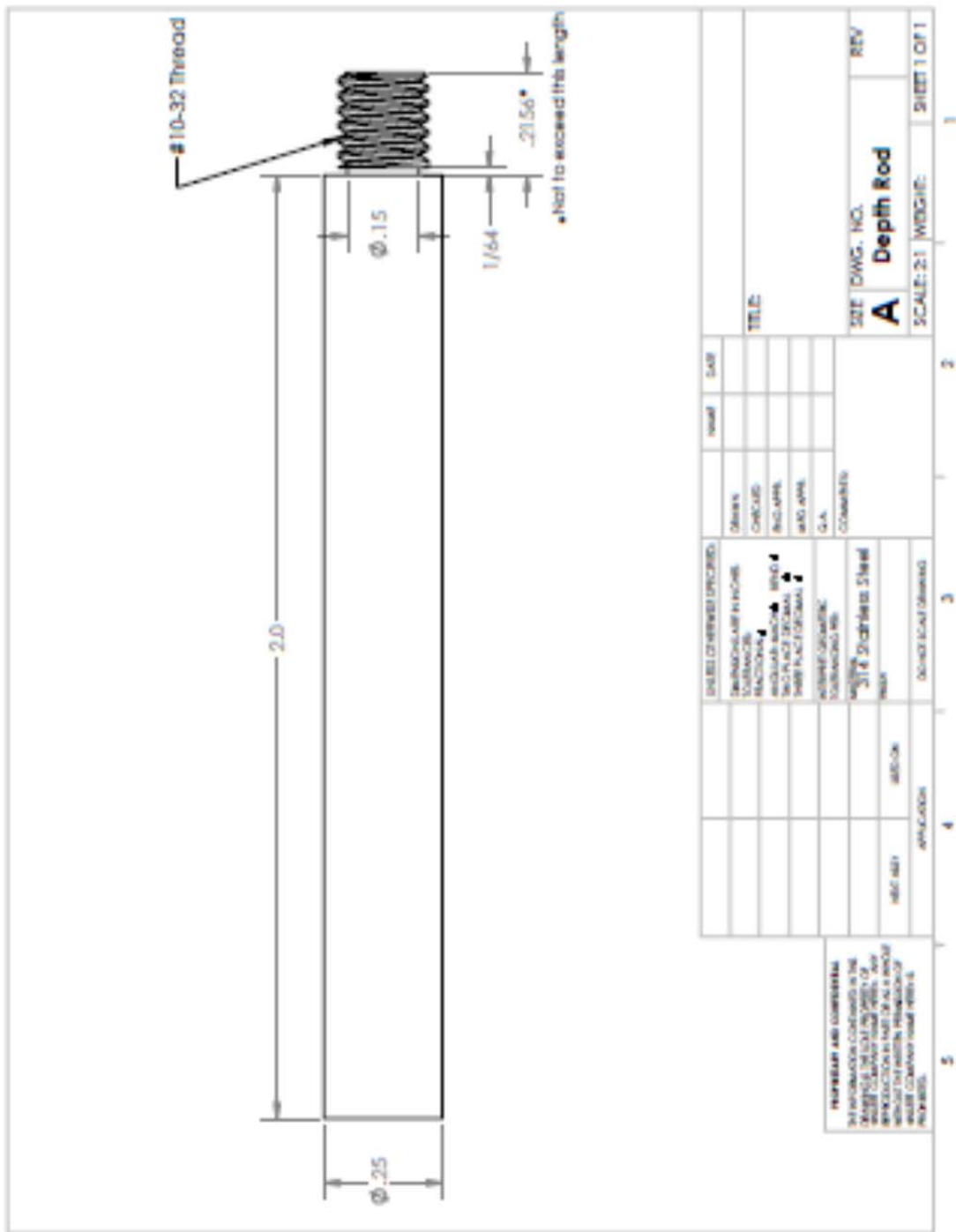


E2E-X8MD□

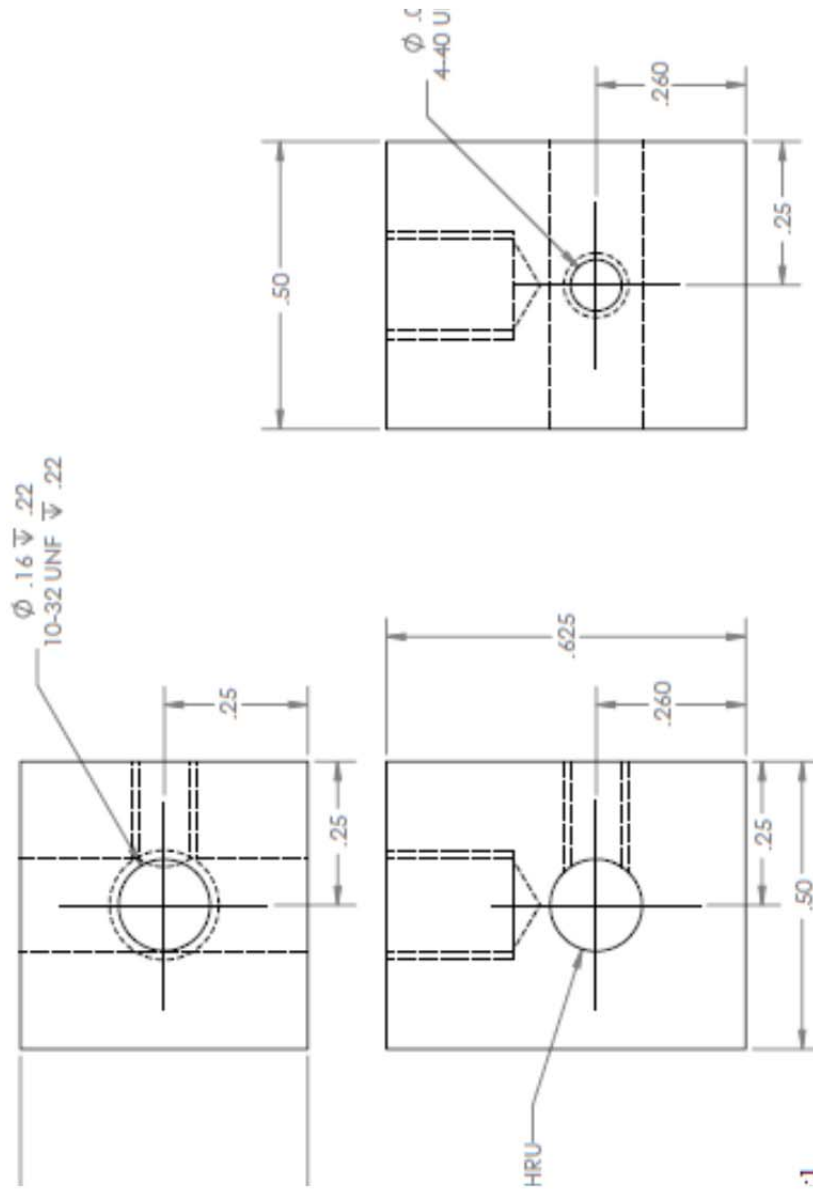


APPENDIX B. DISPLACEMENT SENSOR BRACKET DRAWINGS





<div>REVISIONS AND COMMENTS</div> <div>SEE INFORMATION CONTAINED IN THE DRAWING FOR THE MEANING OF ALL REVISIONS. INDICATIONS IN THIS TABLE ARE TO BE MADE TO THE DRAWING WITHOUT THE NECESSITY OF A REVISION. REVISIONS TO THE DRAWING SHALL BE MADE BY THE DESIGNER OR HIS AUTHORIZED REPRESENTATIVE.</div>	4		3		2		1	
	APP. CODE		DEVELOPER'S NAME		SCALE: 2:1		SHEET 1 OF 1	
	REV. NO.	DATE	REVISION		DATE		REV.	

[illegible]

THIS PAGE INTENTIONALLY LEFT BLANK

APPENDIX C. SAPPHIRE ROD DRAWING



Notes:
.. Flatness: 1/4 wave/inch
.. Scratch/Dig: 60-40
.. Smoothness 10-20 Angstroms

		NAME		DATE	
		DRAWN			
		CHECKED			
		ENG APPR.			
		MFG APPR.			
		Q.A.			
		COMMENTS:			
		INTERPRET GEOMETRIC TOLERANCING PER			
		MATERIAL			
		FINISH			
		DO NOT SCALE DRAWING			
		APPLICATION			
		NEXT ASSY			
		USED ON			
		4		3	
		2		1	
		5		SHEET 1 OF 1	

PROPRIETARY AND CONFIDENTIAL

THE INFORMATION CONTAINED IN THIS DRAWING IS THE SOLE PROPERTY OF <INSERT COMPANY NAME HERE>. ANY REPRODUCTION IN PART OR AS A WHOLE WITHOUT THE WRITTEN PERMISSION OF <INSERT COMPANY NAME HERE> IS PROHIBITED.

SIZE DWG. NO. RE

A

TITLE:

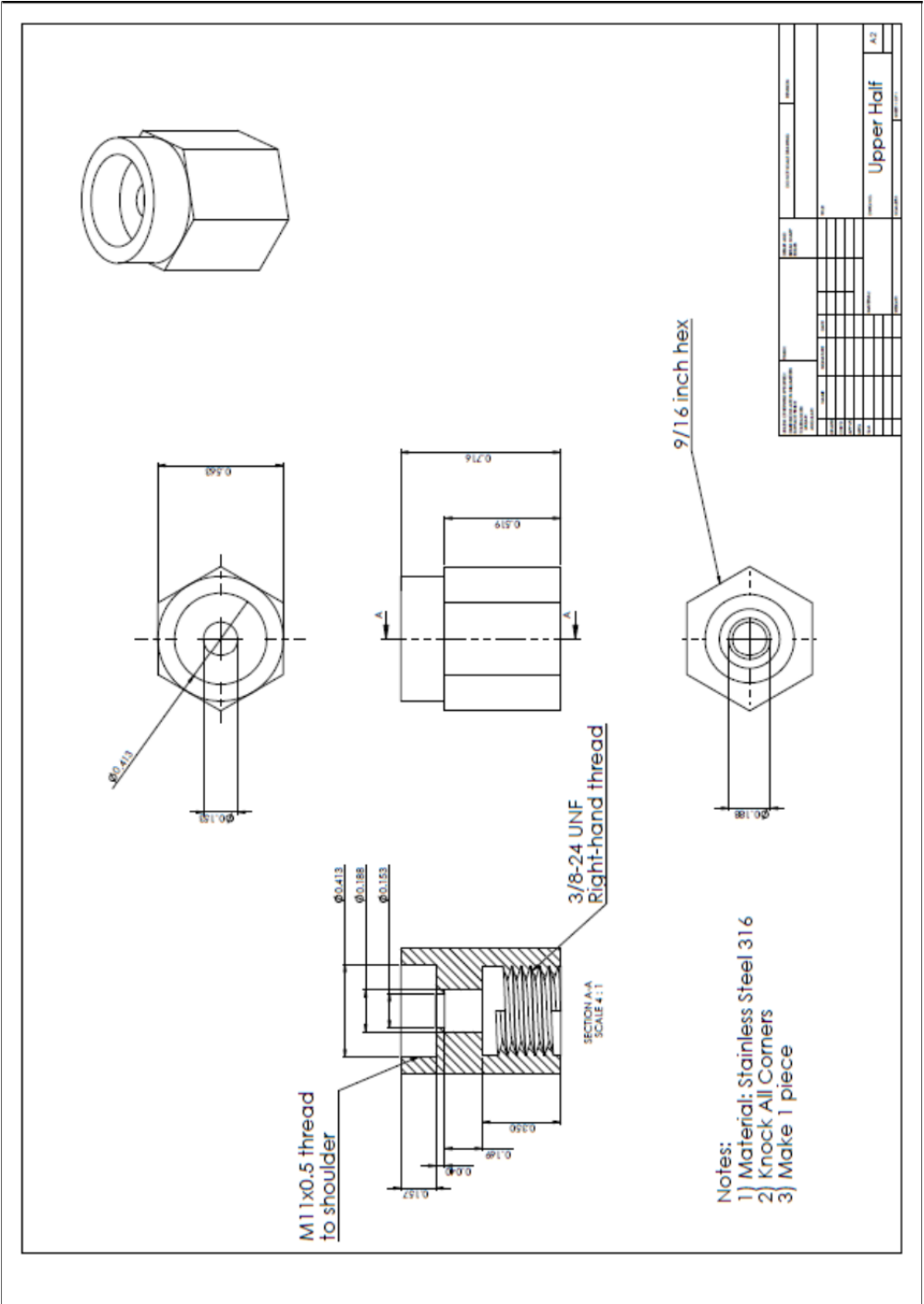
Sapphire Rod Layout

SCALE: 1:1 WEIGHT:

SHEET 1 OF 1

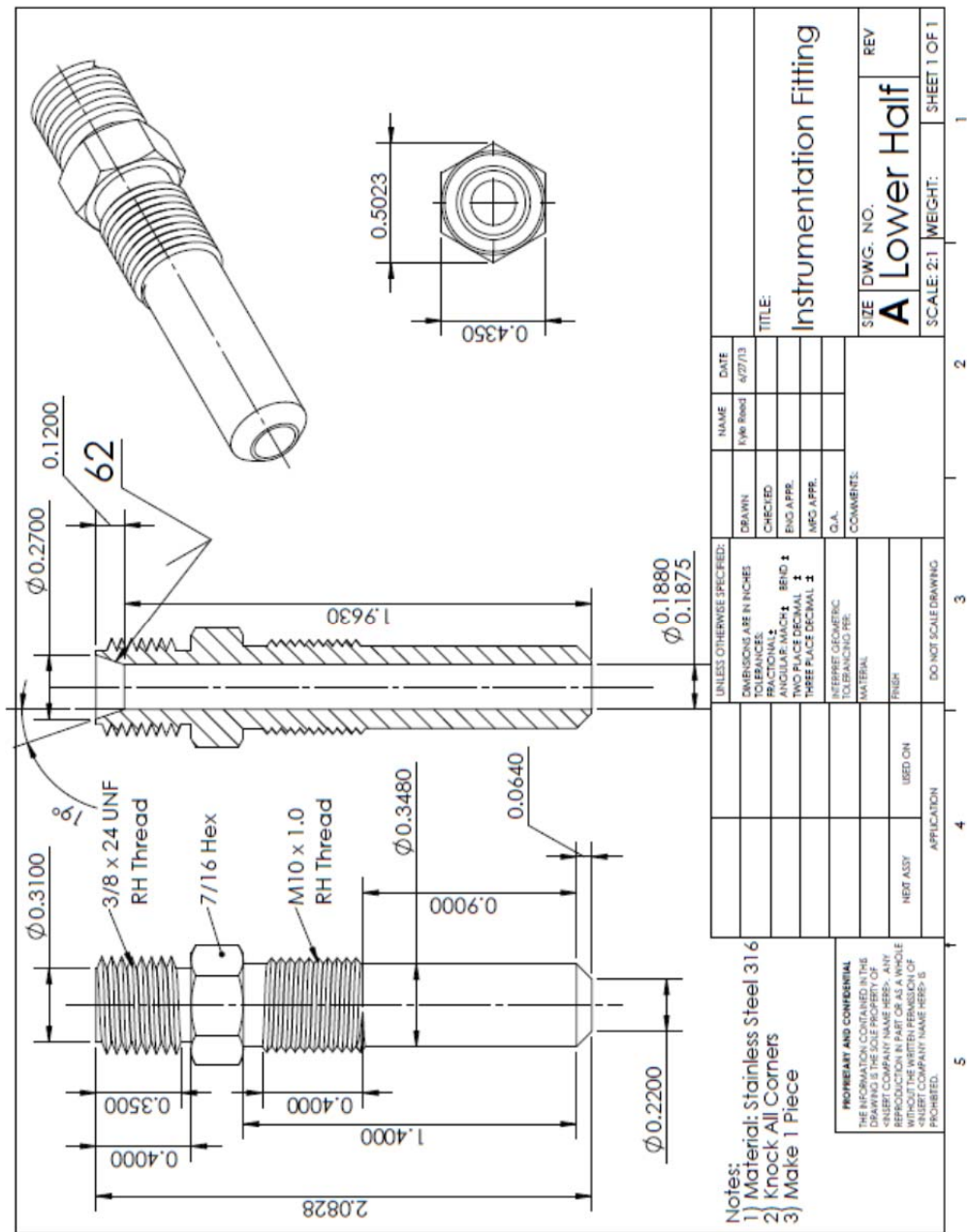
THIS PAGE INTENTIONALLY LEFT BLANK

APPENDIX D. UPPER ROD HOUSING DRAWINGS



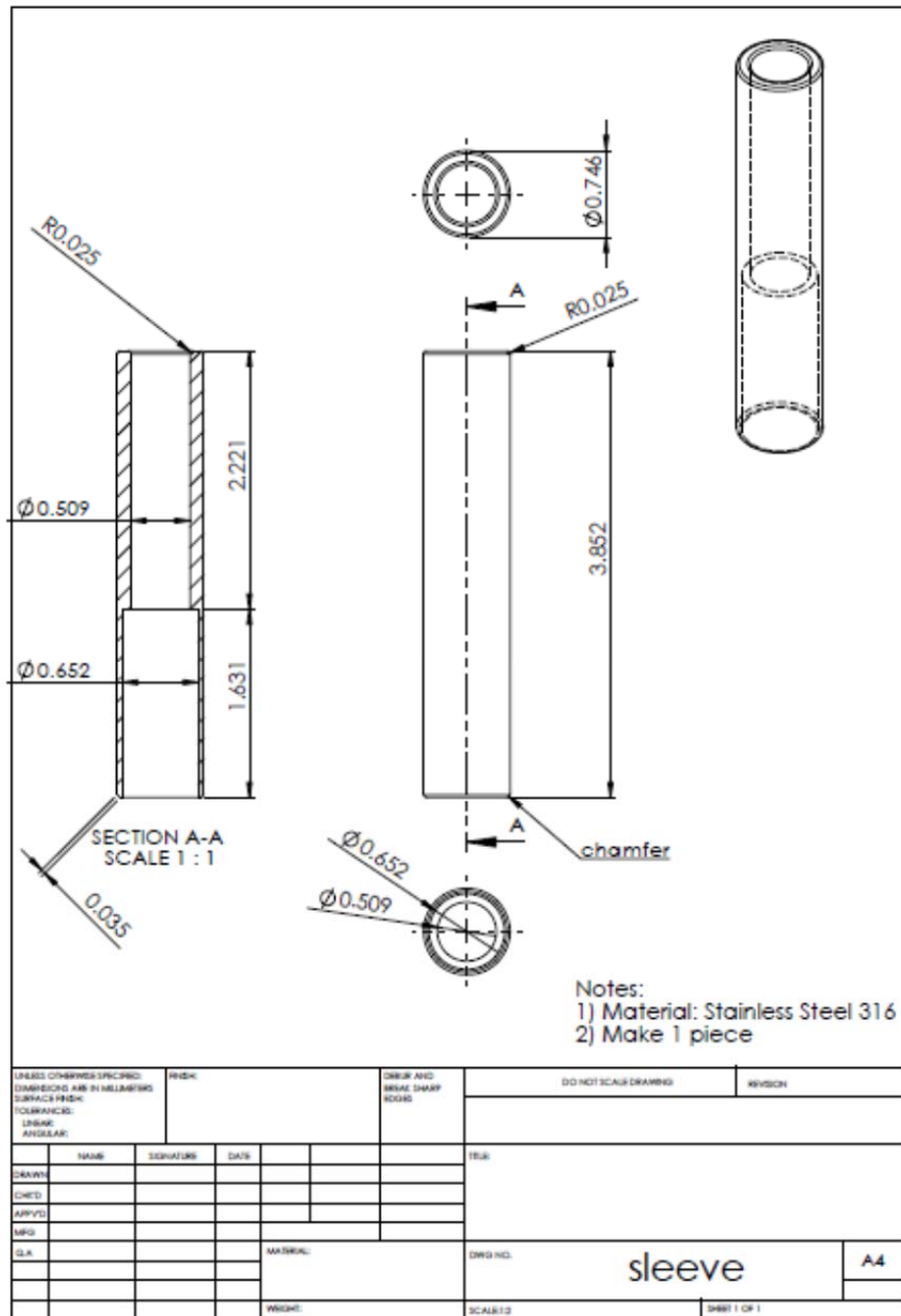
THIS PAGE INTENTIONALLY LEFT BLANK

63



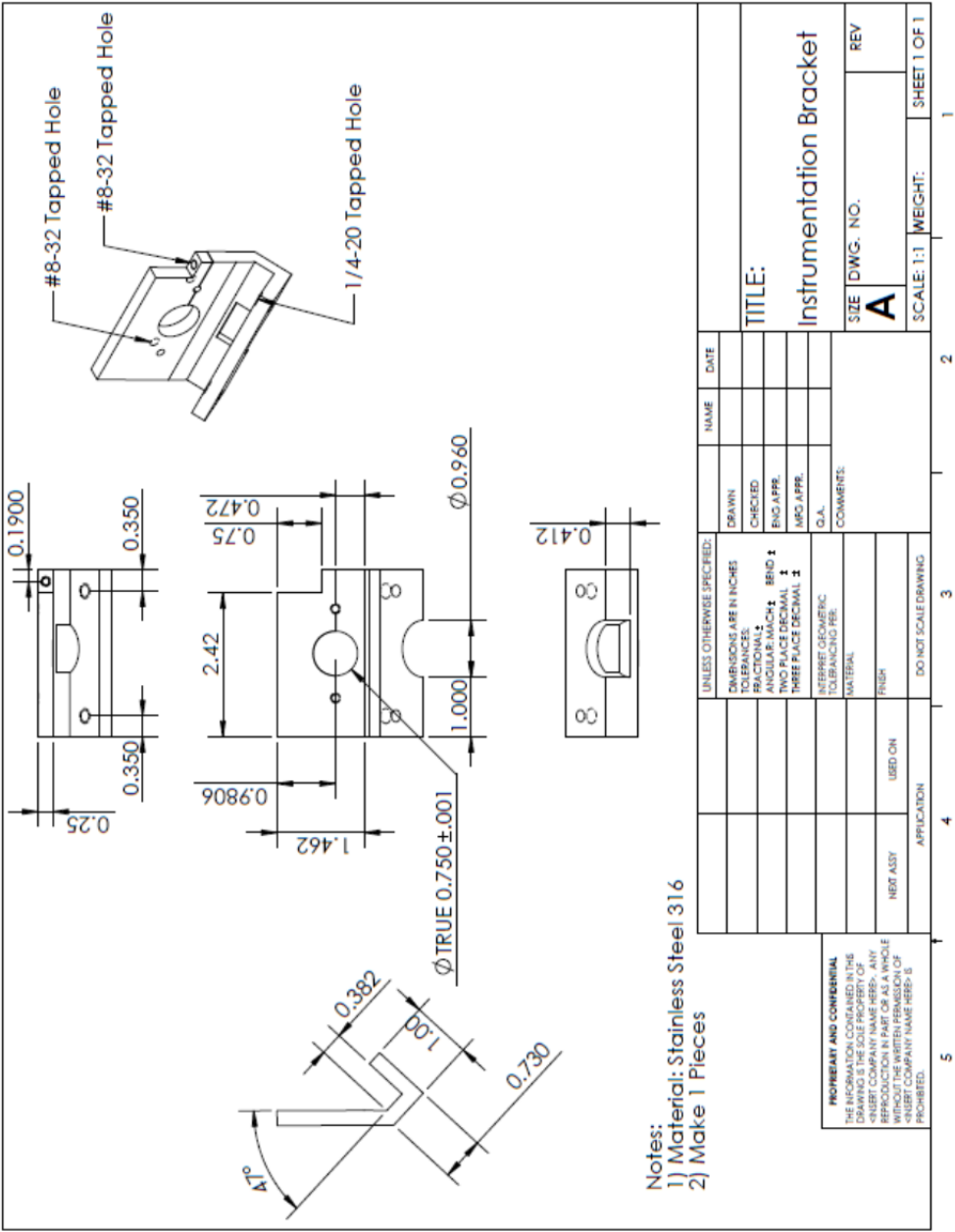
THIS PAGE INTENTIONALLY LEFT BLANK

APPENDIX F. SLEEVE DRAWINGS



THIS PAGE INTENTIONALLY LEFT BLANK

APPENDIX G. INSTRUMENT BRACKET DRAWINGS



THIS PAGE INTENTIONALLY LEFT BLANK

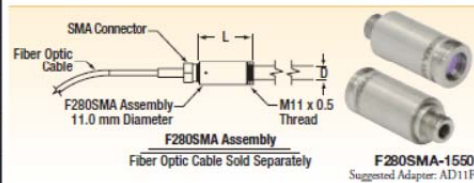
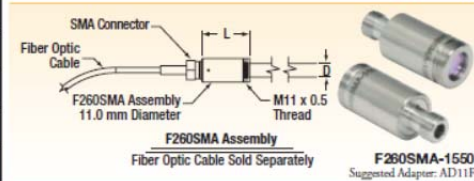
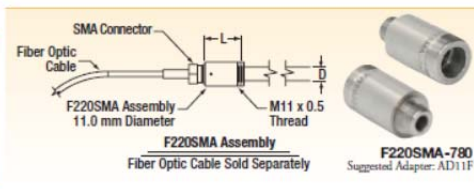
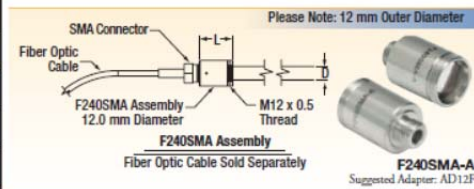
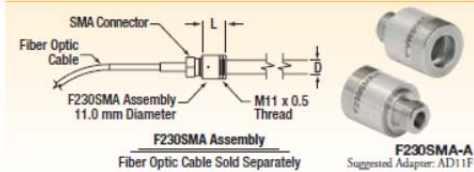
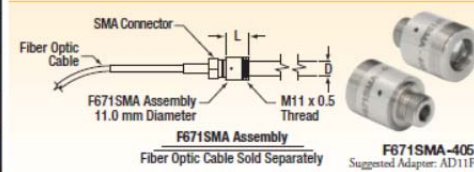
APPENDIX H. COLLIMATION LENSES

Fiber
▼ CHAPTERS
Fiber Patch Cables
Bare Fiber
Fiber Optomechanics
Fiber Components
Test and Measurement
▼ SECTIONS
Collimators
Couplers
WDMs
RGB Combiner
Circulators
Fiber Isolators
Faraday Mirrors
Fiber Attenuators
Polarization Controllers
Optical Switches
Mating Sleeves
Terminating Connectors
Termination

For current pricing,
please see our website.

SMA Fixed Aspheric Lens Fiber Collimation Packages

NEW
versions



Ideal for Coupling
into Multimode Fiber

ITEM # SUFFIX	AR COATING	ALIGNMENT FIBER*
-405	395 - 415 nm	S405
-A	350 - 700 nm	460HP
-B	650 - 1050 nm	SM600
-780	650 - 1050 nm	780HP
-C	1050 - 1620 nm	SMF-28e+
-1064	1050 - 1075 nm	SM980
-1550	1050 - 1620 nm	SMF-28e+

* Fiber not included

SMA-Connectorized Collimation Packages

ITEM #	\$	£	€	RMB	ALIGN λ	D ^a	θ ^b	NA _{LENS}	f ^c	L
F671SMA-405	\$ 158.10	£ 113.83	€ 137.55	¥ 1,260.06	405 nm	0.7 mm	0.041*	0.60	4.02 mm	11.0 mm
F230SMA-A	\$ 137.00	£ 98.64	€ 119.19	¥ 1,091.89	543 nm	0.8 mm	0.049*	0.57	4.34 mm	11.0 mm
F230SMA-B	\$ 137.00	£ 98.64	€ 119.19	¥ 1,091.89	633 nm	0.8 mm	0.056*	0.56	4.43 mm	11.0 mm
F230SMA-C	\$ 137.00	£ 98.64	€ 119.19	¥ 1,091.89	1310 nm	0.8 mm	0.114*	0.53	4.64 mm	11.0 mm
F230SMA-1550	\$ 137.00	£ 98.64	€ 119.19	¥ 1,091.89	1550 nm	0.9 mm	0.128*	0.53	4.67 mm	7.9 mm
F240SMA-A	\$ 144.20	£ 103.82	€ 125.45	¥ 1,149.27	543 nm	1.5 mm	0.027*	0.51	7.86 mm	15.6 mm
F240SMA-B	\$ 144.20	£ 103.82	€ 125.45	¥ 1,149.27	633 nm	1.5 mm	0.031*	0.50	7.93 mm	15.6 mm
F240SMA-780	\$ 144.20	£ 103.82	€ 125.45	¥ 1,149.27	780 nm	1.5 mm	0.032*	0.50	8.00 mm	15.6 mm
F240SMA-C	\$ 144.20	£ 103.82	€ 125.45	¥ 1,149.27	1310 nm	1.5 mm	0.065*	0.49	8.13 mm	15.6 mm
F240SMA-1550	\$ 144.20	£ 103.82	€ 125.45	¥ 1,149.27	1550 nm	1.6 mm	0.073*	0.49	8.18 mm	12.7 mm
F220SMA-A	\$ 130.80	£ 94.18	€ 113.80	¥ 1,042.48	543 nm	2.0 mm	0.020*	0.25	10.90 mm	18.2 mm
F220SMA-B	\$ 130.80	£ 94.18	€ 113.80	¥ 1,042.48	633 nm	2.1 mm	0.022*	0.25	10.99 mm	18.2 mm
F220SMA-780	\$ 130.80	£ 94.18	€ 113.80	¥ 1,042.48	780 nm	2.1 mm	0.030*	0.25	11.07 mm	18.2 mm
F220SMA-1064	\$ 130.80	£ 94.18	€ 113.80	¥ 1,042.48	1064 nm	2.4 mm	0.032*	0.25	11.17 mm	18.2 mm
F220SMA-C	\$ 130.80	£ 94.18	€ 113.80	¥ 1,042.48	1310 nm	2.0 mm	0.047*	0.24	11.23 mm	18.2 mm
F220SMA-1550	\$ 130.80	£ 94.18	€ 113.80	¥ 1,042.48	1550 nm	2.1 mm	0.053*	0.24	11.29 mm	15.6 mm
F260SMA-A	\$ 126.70	£ 91.22	€ 110.23	¥ 1,009.80	543 nm	2.8 mm	0.014*	0.17	15.01 mm	22.2 mm
F260SMA-B	\$ 126.70	£ 91.22	€ 110.23	¥ 1,009.80	633 nm	2.8 mm	0.016*	0.16	15.15 mm	22.2 mm
F260SMA-C	\$ 126.70	£ 91.22	€ 110.23	¥ 1,009.80	1310 nm	2.8 mm	0.034*	0.16	15.52 mm	22.2 mm
F260SMA-1550	\$ 126.70	£ 91.22	€ 110.23	¥ 1,009.80	1550 nm	3.0 mm	0.038*	0.16	15.58 mm	19.1 mm
F280SMA-A	\$ 125.00	£ 90.00	€ 108.75	¥ 996.25	543 nm	3.3 mm	0.012*	0.15	18.07 mm	25.0 mm
F280SMA-B	\$ 125.00	£ 90.00	€ 108.75	¥ 996.25	633 nm	3.4 mm	0.014*	0.15	18.24 mm	25.0 mm
F280SMA-C	\$ 125.00	£ 90.00	€ 108.75	¥ 996.25	1310 nm	3.4 mm	0.028*	0.15	18.67 mm	25.0 mm
F280SMA-1550	\$ 125.00	£ 90.00	€ 108.75	¥ 996.25	1550 nm	3.6 mm	0.032*	0.15	18.75 mm	22.1 mm

^aTheoretical 1/e² diameter at 1 focal length from lens at the alignment wavelength using the alignment fiber type

^bMeasured full beam angle of divergence

^cEffective focal length of the aspheric lens at the alignment wavelength

1100

www.thorlabs.com

THORLABS

THIS PAGE INTENTIONALLY LEFT BLANK

APPENDIX I. HR 2000 SPECTROMETER SPECIFICATIONS

Appendix B

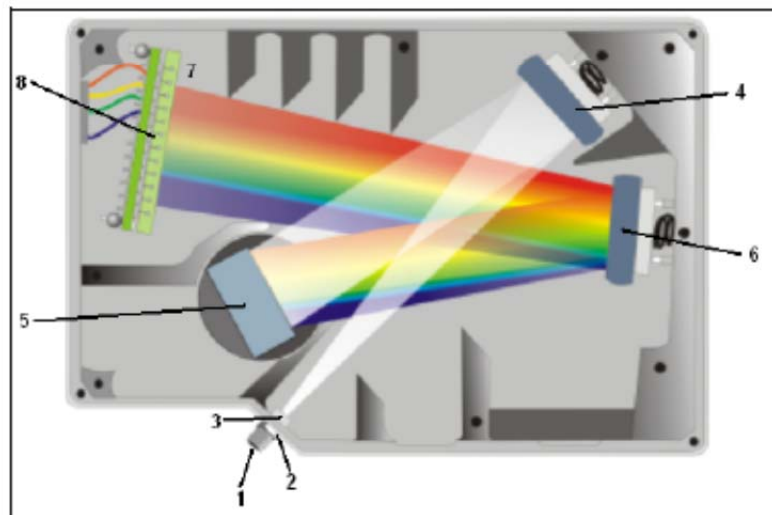
Specifications

Overview

This appendix contains information on spectrometer operation, specifications, and system compatibility. It also includes accessory connector pinout diagrams and pin-specific information.

How the HR2000+ Works

Below is a diagram of how light moves through the optical bench of an HR2000+ Spectrometer. The optical bench has no moving parts that can wear or break; all the components are fixed in place at the time of manufacture. Items with an asterisk (*) are user-specified.



HR2000+ Spectrometer with Components

See [HR2000+ Components Table](#) on the following page for an explanation of the function of each numbered component in the HR2000+ Spectrometer in this diagram.

HR2000+ Components Table

Ocean Optics permanently secures all components in the HR2000+ at the time of manufacture. Only Ocean Optics technicians can replace interchangeable components, where noted.

Item	Name	Description
1	SMA Connector	Secures the input fiber to the spectrometer. Light from the input fiber enters the optical bench through this connector.
2	Slit	A dark piece of material containing a rectangular aperture, which is mounted directly behind the SMA Connector. The size of the aperture regulates the amount of light that enters the optical bench and controls spectral resolution. You can also use the HR2000+ without a Slit. In this configuration, the diameter of the fiber connected to the HR2000+ determines the size of the entrance aperture. Only Ocean Optics technicians can change the Slit.
3	Filter	Restricts optical radiation to pre-determined wavelength regions. Light passes through the Filter before entering the optical bench. Both bandpass and longpass filters are available to restrict radiation to certain wavelength regions. Only Ocean Optics technicians can change the Filter.
4	Collimating Mirror	Focuses light entering the optical bench towards the Grating of the spectrometer. Light enters the spectrometer, passes through the SMA Connector, Slit, and Filter, and then reflects off the Collimating Mirror onto the Grating.
5	Grating	Diffraction light from the Collimating Mirror and directs the diffracted light onto the Focusing Mirror. Gratings are available in different groove densities, allowing you to specify wavelength coverage and resolution in the spectrometer. Only Ocean Optics technicians can change the Grating.
6	Focusing Mirror	Receives light reflected from the Grating and focuses the light onto the CCD Detector or L2 Detector Collection Lens (depending on the spectrometer configuration).
7	L2 Detector Collection Lens	An optional component that attaches to the CCD Detector. It focuses light from a tall slit onto the shorter CCD Detector elements. The L2 Detector Collection Lens should be used with large diameter slits or in applications with low light levels. It also improves efficiency by reducing the effects of stray light. Only Ocean Optics technicians can add or remove the L2 Detection Collection Lens.
8	CCD Detector (UV or VIS)	Collects the light received from the Focusing Mirror or L2 Detector Collection Lens and converts the optical signal to a digital signal. Each pixel on the CCD Detector responds to the wavelength of light that strikes it, creating a digital response. The spectrometer then transmits the digital signal to the OOIBase32 application.

HR2000+ Specifications

The following sections provide specification information for the CCD detector in the HR2000+, as well as the HR2000+ Spectrometer itself. HR2000+CG-UV-NIR specifications are listed in *Appendix C*: [Error! Reference source not found.](#)

CCD Detector Specifications

Specification	Value
Detector	Sony ILX-511B linear silicon CCD array
No. of elements	2048 pixels
Sensitivity	75 photons per count at 400 nm 41 photons per count at 800 nm
Pixel size	14 μm x 200 μm
Pixel well depth	65 Ke-
Signal-to-noise ratio	250:1 (at full signal)
A/D resolution	14 bit
Dark noise	3.2 RMS counts
Corrected linearity	>99.8%
Maximum pixel rate	Rate at which pixels are digitized is 1 MHz

HR2000+ Spectrometer

Specification	Value
Dimensions	148.6 mm x 104.8 mm x 45.1 mm
Weight	570 g
Power consumption	220 mA @ 5 VDC
Detector	2048-element linear silicon CCD array
Detector range	200-1100 nm
Gratings	14 gratings available

B: HR2000+ Specifications

Specification	Value
Entrance aperture	5, 10, 25, 50, 100 or 200 μm wide slits
Order-sorting filters	Installed longpass and bandpass filters
Focal length	f/4, 101 mm
Optical resolution	Depends on grating and size of entrance aperture
Stray light	<0.05% at 600 nm; <0.10% at 435 nm
Dynamic range	2×10^8 (system); 1300:1 for a single acquisition
Fiber optic connector	SMA 905 to single-strand optical fiber (0.22 NA)
Data transfer rate:	
USB 2.0 Port	Full scans into memory every 1 millisecond
Serial Port	Full scans into memory every 600 milliseconds
Integration time	1 ms to 65 seconds
Interfaces	USB 2.0, 480 Mbps (USB 1.1 compatible); RS-232 (2-wire); SPI (3-wire); I ² C Inter-Integrated Circuit 2-wire serial bus
Operating systems:	
USB Port	Windows 2000/XP, Mac OS X, and Linux
Serial Port	Any 32-bit Windows operating system
Onboard GPIO	10 user-programmable digital I/Os
Analog channels	One 13-bit analog input and one 9-bit analog output

System Compatibility

The following sections provide information on hardware and software requirements for the HR2000+.

Compatibility for Desktop or Notebook PCs

To use the HR2000+, you must have a PC that meets the following minimum requirements:

- Operating systems: Windows 2000/XP, Mac OS X, or Linux with USB port; any 32-bit or 64-bit Windows OS with serial port
- Computer interfaces: USB 2.0 @ 480 Mbps; RS-232 (2-wire) @ 115.2 K baud
- Peripheral interfaces: I²C inter-integrated circuit

APPENDIX J. SONY CCD LINEAR IMAGE SENSOR DATA SHEET

SONY

ILX511

2048-pixel CCD Linear Image Sensor (B/W)

Description

The ILX511 is a rectangular reduction type CCD linear image sensor designed for bar code POS hand scanner and optical measuring equipment use. A built-in timing generator and clock-drivers ensure single 5 V power supply for easy use.

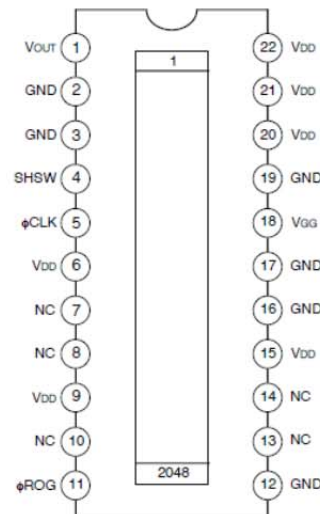
Features

- Number of effective pixels: 2048 pixels
- Pixel size: $14\ \mu\text{m} \times 200\ \mu\text{m}$ ($14\ \mu\text{m}$ pitch)
- Single 5 V power supply
- Ultra-high sensitivity
- Built-in timing generator and clock-drivers
- Built-in sample-and-hold circuit
- Maximum clock frequency: 2MHz

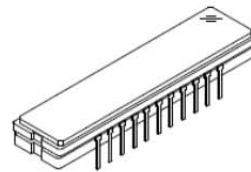
Absolute Maximum Ratings

- Supply voltage V_{DD} 6 V
- Operating temperature -10 to $+60$ °C
- Storage temperature -30 to $+80$ °C

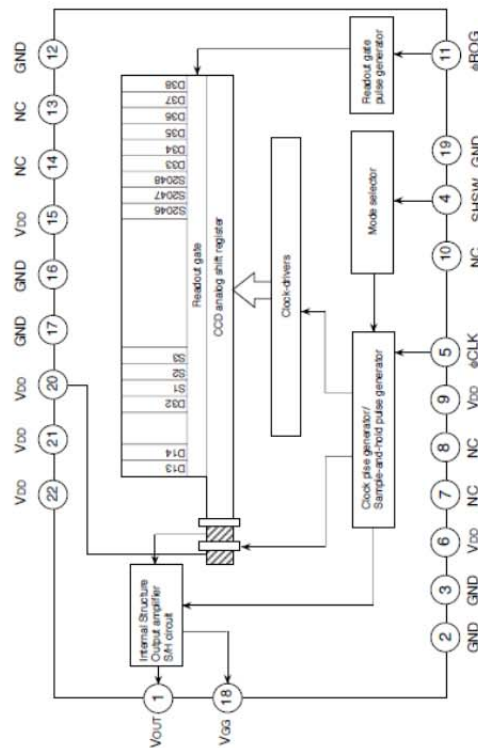
Pin Configuration (Top View)



22 pin DIP (Plastic)



Block Diagram



Sony reserves the right to change products and specifications without prior notice. This information does not convey any license by any implication or otherwise under any patents or other right. Application circuits shown, if any, are typical examples illustrating the operation of the devices. Sony cannot assume responsibility for any problems arising out of the use of these circuits.

Electro-optical Characteristics

(Ta = 25 °C, VDD = 5 V, Clock frequency: 1 MHz, Light source = 3200 K, IR cut filter: CM-500S (t = 1.0 mm), Without S/H mode)

Item	Symbol	Min.	Typ.	Max.	Unit	Remarks
Sensitivity 1	R1	150	200	250	V/(lx · s)	Note 1
Sensitivity 2	R2	—	1800	—	V/(lx · s)	Note 2
Sensitivity nonuniformity	PRNU	—	5.0	10.0	%	Note 3
Saturation output voltage	VSAT	0.6	0.8	—	V	—
Dark voltage average	VDRK	—	3.0	6.0	mV	Note 4
Dark signal nonuniformity	DSNU	—	6.0	12.0	mV	Note 4
Image lag	IL	—	1	—	%	Note 5
Dynamic range	DR	—	267	—	—	Note 6
Saturation exposure	SE	—	0.004	—	lx · s	Note 7
5 V current consumption	I VDD	—	5.0	10.0	mA	—
Total transfer efficiency	TTE	92.0	98.0	—	%	—
Output impedance	Zo	—	250	—	Ω	—
Offset level	Vos	—	2.8	—	V	Note 8

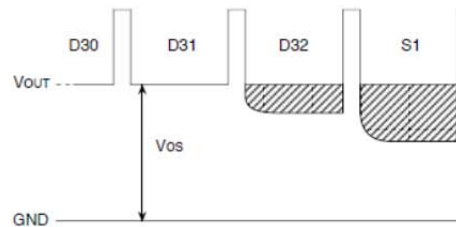
Note)

- For the sensitivity test light is applied with a uniform intensity of illumination.
- Light source: LED $\lambda = 660\text{nm}$
- PRNU is defined as indicated below. Ray incidence conditions are the same as for Note 1.

$$\text{PRNU} = \frac{(V_{\text{MAX}} - V_{\text{MIN}})/2}{V_{\text{AVE}}} \times 100 (\%)$$

The maximum output of all the valid pixels is set to VMAX, the minimum output to VMIN and the average output to VAVE.

- Integration time is 10ms.
- Typical value is used for clock pulse and readout pulse. VOUT = 500 mV.
- $\text{DR} = \text{VSAT}/\text{VDRK}$. When optical integration time is shorter, the dynamic range sets wider because dark voltage is in proportion to optical integration time.
- $\text{SE} = \text{VSAT}/\text{R1}$
- Vos is defined as indicated below.



LIST OF REFERENCES

- [1] Department of Defense, Fiscal year 2012 operational energy annual report, Rep. C-584E097, Sep. 2013.
- [2] Energy, environment and climate change. (n.d.). U.S. Department of the Navy. [Online]. <http://greenfleet.DoDlive.mil/energy/>. Accessed Jun. 17, 2014
- [3] J. Fu, and S. Q. Turn. “Characteristics and stability of neat and blended Hydroprocessed Renewable Diesel,” *Energy&Fuels*, vol. 28, no. 6, pp.3899-3907, May, 2014.
- [4] Office of Naval Research, “Fuel data on HRD and F-76,” unpublished, July 2012
- [5] J. Petersen, D. Seivwright, P. Canton, and K. Millsaps. “Combustion characterization and ignition delay modeling of low and high-cetane alternative diesel fuels in a marine diesel engine,” *Energy & Fuels*, vol. 28, no. 8, pp. 5463–5471, Jul., 2014.
- [6] T. Edwards, D. Minus, W. Harrison, E. Corporan, M. DeWitt, S. Zabarnick, and L. Balster. “Fischer-Tropsch jet fuels – Characterization for advanced aerospace applications,” presented at 40th AIAA/ASME/SAD/ASEE Joint Propulsion Conference and Exhibit, Fort Lauderdale, Florida, 2004.
- [7] M. Dry, “High quality diesel via the Fischer–Tropsch process—a review,” *J. of Chemical Technology and Biotechnology*, vol. **77**, no.1, pp. 43–50, Jan. 2002.
- [8] D. Halliday, R. Resnick, and J. Walker, “*Fundamentals of Physics*, 6th edition,” Hoboken, New Jersey: Wiley, 2002, pp. 1128-1129.
- [9] A. Boehman, D. Morris, and J. Szybist, “The impact of the bulk modulus of diesel fuels on fuel injection timing,” *Energy & Fuels*, vol. 10, no. 6, pp. 1877–1882, Jun. 2004.
- [10] J. Szybist, J. Song, and M. Alam, “Biodiesel combustion, emissions and emission control,” *Fuel Processing Technology*, vol. 88, no. 7, pp. 679–691, Jul. 2007.
- [11] J. Szybist, S. Kirby, and A. Boehman, “NOX emissions of alternative diesel fuels: A comparative analysis of biodiesel and FT diesel,” *Energy & Fuels*, vol. 19, no. 4, pp. 1484–1492, Apr. 2005.
- [12] Bulk Modulus and Fluid Elasticity. (n.d.). The Engineering Toolbox. [Online]. http://www.engineeringtoolbox.com/bulk-modulus-elasticity-d_585.html, Accessed Sept. 2, 2014

- [13] C. A. Moses, and P.N. Roets, (2009, Apr. 16). Properties, characteristics, and combustion performance of Sasol fully synthetic jet fuel. *J. of Eng. for Gas Turbines and Power* [Online]. 131(4). Available: <http://gasturbinespower.asmedigitalcollection.asme.org/article.aspx?articleid=1474688>
- [14] Southwest Research Institute, "Bulk Modulus Data for F-76 and HRD," unpublished, September 2014
- [15] K. Millsaps, P. Caton, D. Seivwright, J. Petersen, and A. Paz, "Combustion characteristics of HRD/SPK alternative diesel fuels and F-76 blends in a marine diesel engine," presented at ONR Alternative Fuels Meeting, 2013.
- [16] J. H. Petersen, "Combustion heat release rate comparison of algae hydroprocessed renewable diesel to F-76 in a two-stroke diesel engine," M. S. thesis, Dept. Mech. and Aero Eng., Naval Postgraduate School, Monterey, CA, 2012.
- [17] P. Lacey, and S. Howell, "Fuel lubricity reviewed," SAE paper number 982567, Oct. 1998
- [18] K. Sugiyama, I. Goto, and K. Kitano, "Effects of hydrotreated vegetable oil (HVO) as renewable diesel fuel on combustion and exhaust emissions in diesel engine," *SAE Int. J. of Fuels and Lubricants*, vol. 5, no. 1, pp. Jan. 2012 .
- [19] M. Kuronen, S. Mikkonen, and P. Aakko, "Hydrotreated vegetable oil as fuel for heavy duty diesel engines," SAE Technical Paper #2007-01-4031, 2007.
- [20] T. Murtonen, P. Aakko, and M. Kuronen, "Emissions with heavy-duty diesel engines and vehicles using FAME, HVO and GTL fuels with and without DOC POC aftertreatment," *SAE Int. J. of Fuels and Lubricants*, vol. 2, no. 2, pp. 147–166, Feb. 2010.
- [21] M. Happonen, J. Heikkilä, and T. Murtonen, "Reductions in particulate and NO X emissions by diesel engine parameter adjustments with HVO fuel," *Environmental Sci. & Technology*, vol. 46, no. 11, pp. 6198–6204, Nov. 2012.
- [22] A. Abu-Jrai, A. Tsolakis, and K. Theinnoi, "Effect of gas-to-liquid diesel fuels on combustion characteristics, engine emissions, and exhaust gas fuel reforming. Comparative study," *Energy & Fuels*, vol. 20, no. 6, pp. 2377–2384, Jun. 2006.
- [23] A. Abu-Jrai, J. Rodríguez-Fernández, and A. Tsolakis, "Performance, combustion and emissions of a diesel engine operated with reformed EGR. Comparison of diesel and GTL fuelling," *Fuel*, vol. 88, no. 6, pp. 1031–1041, Jun. 2009.

- [24] Y. Lin, Y. Lin, and C. Zhang, "Evaluation of combustion performance of a coal-derived synthetic jet fuel," in *Proc. ASME Turbo Expo 2012: Turbine Technical Conf. and Expo.*, Copenhagen, Denmark, 2012, pp. 569–576.
- [25] D. M. Korres, D. Karonis, E. Lois, M. B. Linck, and A. K. Gupta, "Aviation fuel JP-5 and biodiesel on a diesel engine," *Fuel*, vol.87, no.1, pp. 70-78, Jan. 2008.
- [26] C. Moses, "Comparative evaluation of semi-synthetic jet fuels," Univ. Tech. Corp., Dayton, OH, CRC Project AV-2–04a, Sep. 2008.
- [27] M. Tat, and J. Van Gerpen, "Measurement of biodiesel speed of sound and its impact on injection timing," Natl. Renewable Energy Lab., NREL/SR-510–31462, Feb. 2003.
- [28] A. Boehman, M. Alam, and J. Song, "Fuel formulation effects on diesel fuel injection, combustion, emissions and emission control," presented at Diesel Engine Emissions Reduction Conf., Newport, RI, 2003,
- [29] M. Tat, J. Van Gerpen, and P. Wang, "Fuel property effects on injection timing, ignition timing, and oxides of nitrogen emissions from biodiesel-fueled engines," presented at Trans. of ASAE/CSAE Annu. Int. Meeting, Ottawa, Canada, 2004.
- [30] F. W. D. Rost, *Quantitative Fluorescence Microscopy*, Cambridge England: Cambridge Univ. Press, 1991, p. 418–419.
- [31] Laser-Induced Fluorescence. (n.d.). Wikipedia. Available: http://commons.wikimedia.org/wiki/File:Laser-induced_fluorescence.png#mediaviewer/File:Laser-induced_fluorescence.png. Accessed Sep. 03, 2014.
- [32] J. Prieto, F. Arbeloa, and V. Martínez, "Photophysical properties of the pyrromethene 597 dye: solvent effect," *The J. of Physical Chemistry A*, vol. 108, no. 26, pp. 5503–5508. Jun. 2004
- [33] C. Brown, private communication, Sep. 2014
- [34] Pyrromethene 597. (n.d.). Exciton Corporation. [Online]. <http://www.photonicsolutions.co.uk/datasheets/exci/pyrromethene%20597.pdf>. Accessed Sep. 03, 2014
- [35] K. Millsaps, C. Brophy, D. Seivwright, "Bracketing of injection event to determine the effect of bulk modulus on engine performance," presented at ONR Alternative Fuels Meeting, 2014
- [36] *Series 53 Service Manual Detroit Diesel Engines*, General Motors Corporation, Detroit, Michigan, 1973.

- [37] Standard Proximity Sensor E2E Data Sheet. (n.d.). Omron Corporation. [Online]. http://www.ia.omron.com/data_pdf/cat/e2e_ds_e_9_2_csm446.pdf. Accessed Sep. 18, 2014
- [38] S. Mittl, private communication, Sep. 16, 2014
- [39] G4 Diode Pumped Solid State Laser Data Sheet. (n.d.). Elforlight Limited. [Online]. http://www.elforlight.com/_assets/PDF/DataSheets/G4.pdf. Accessed Sep. 18, 2014
- [40] Dichroic Cage Cube Catalog Image. (n.d.). Thorlabs Incorporated. [Online]. http://www.thorlabs.us/newgrouppage9.cfm?objectgroup_id=6079. Accessed Sep. 18, 2014
- [41] DMLP567 Transmission and Reflectance Data. (n.d.). Thorlabs Incorporated. [Online]. http://www.thorlabs.us/newgrouppage9.cfm?objectgroup_id=3313#3631. Accessed September 18, 2014
- [42] PDA36A Catalog Page. (n.d.). Thorlabs Incorporated. [Online]. <http://www.thorlabs.us/catalogpages/V21/1573.PDF>. Accessed Sep. 14, 2014
- [43] UV/VIS Bandpass & Laser Line Filters: 340 - 694.3 Nm Center Wavelength. (n.d.). Thorlabs Incorporated. [Online]. http://www.thorlabs.us/newgrouppage9.cfm?objectgroup_id=1001&pn=FB590-10#5414. Accessed Sep.14, 2014
- [44] FT800UMT Fiber Optic Cable Catalog Page. (n.d.). Thorlabs Incorporated. [Online]. <http://www.thorlabs.us/catalogpages/V21/1061.PDF>. Accessed Sep. 13, 2014
- [45] M40L02 Fiber Optic Cable Catalog Page. (n.d.). Thorlabs Incorporated. [Online]. <http://www.thorlabs.us/catalogpages/V21/1014.PDF>. Accessed September 10, 2014

INITIAL DISTRIBUTION LIST

1. Defense Technical Information Center
Ft. Belvoir, Virginia
2. Dudley Knox Library
Naval Postgraduate School
Monterey, California